IMPROVED TECHNIQUES FOR STATISTICAL ANALYSIS OF THE ENVELOPE OF BACKSCATTERED ULTRASOUND USING THE HOMODYNED K DISTRIBUTION

BY

DAVID P. HRUSKA

B.S., University of Illinois at Urbana-Champaign, 2007

THESIS

Submitted in partial fulfillment of the requirements
for the degree of Master of Science in Electrical and Computer Engineering
in the Graduate College of the
University of Illinois at Urbana-Champaign, 2009

Urbana, Illinois

Adviser:

Assistant Professor Michael L. Oelze

ABSTRACT

Biomedical ultrasound is a prominent imaging modality for diagnostics. Conventional ultrasonic imaging is qualitative in nature with spatial resolution up to hundreds of micrometers. Quantitative ultrasound techniques based on ultrasonic backscatter can provide estimates describing tissue microstructure. Improving quantitative ultrasound techniques will result in improved diagnostic capabilities of ultrasound.

Quantitative techniques were developed and assessed based on the envelope of backscattered ultrasound. The envelope of backscattered ultrasound can be modeled as the superposition of the scattered signals from individual scatterers in the medium being interrogated. As such, the envelope signal is statistical in nature. By applying a model to the amplitude distribution of the envelope, information about the sub-resolution material properties such as the scatterer number density and organizational structure can be obtained.

The homodyned K distribution was used to model the envelope of backscattered ultrasound. An efficient parameter estimation algorithm was developed and tested through simulations and experiments. Techniques to reduce estimate bias and variance were assessed. The diagnostic potential of tissue characterization based on envelope statistics was evaluated.

ACKNOWLEDGMENTS

First of all, the support of my research adviser Michael L. Oelze must be acknowledged. A number of investigators including Jennifer King, Michael King, Roberto Lavarello, Ernest Madsen, Sandhya Sarwate, and Jun Song were involved in the construction, scanning, and processing of the phantoms described in Sections 3.3.1, 3.3.2, and 4.4.2.3. Roberto Lavarello contributed a number of ideas and suggestions, particularly the analysis of the gradient which led to the developments in Section 2.3. Finally, this work was made possible by grant number CA111289 from the National Institutes of Health (NIH).

TABLE OF CONTENTS

CHAPTER 1
INTRODUCTION

1.1 Motivation

Diagnostic medical ultrasound is a fast, safe, noninvasive, and low-cost imaging modality [1], [2]. This makes ultrasound an attractive approach for the detection and monitoring of disease. In fact, the use of ultrasound to observe morphological structures associated with disease dates back over 55 years [3].

An even more robust diagnostic capability for ultrasonic imaging is possible if tissue microstructure could be imaged. However, the histopathologic features used to make diagnoses may be as small as 5 μm [1]. Assuming a propagation speed of 1540 m/s, the frequency required to achieve a 5 μm wavelength is over 300 MHz. Besides the present technical difficulties associated with the production of high frequency ultrasound, properties of propagation in tissues, e.g., attenuation, limit the penetration depth used in practice. Typical clinical ultrasound systems employ frequencies in the range of 1 to 15 MHz [4], [5]. A focused (f/2.4) 10 MHz linear array transducer typical of current clinical systems has a penetration depth of roughly 5 cm assuming a linear attenuation coefficient of 0.5 dB/(MHz·cm). Considering only diffraction effects, the axial resolution is 0.33 mm and the lateral resolution is 0.26 mm [6]. Therefore, the direct imaging of tissue microstructure on the scale of 10s of micrometers or less is not feasible, and alternative approaches have to be used instead. By applying a statistical model to the amplitude distribution of the envelope of backscattered ultrasound, some information about the sub-

resolution tissue microstructure can be obtained. We hypothesize that this information is useful for the diagnosis and monitoring of disease.

1.2 Envelope Statistics Models

A number of models for the statistics of the envelope of acoustic and optical signals have been proposed over the past few decades with applications to sea echo [7], medical ultrasound [8], and laser [9]. Some of these distributions include the Rayleigh distribution, the K distribution, and the homodyned K distribution. Because the derivations of these distributions have been covered extensively in the literature (e.g., [10], [11]), only a brief review is given.

1.2.1 Rayleigh distribution

The Rayleigh distribution arises when a large number of nearly identical and randomly located scatterers contribute to the echo signal [12]. The probability density function (pdf) is given by

$$p_A(A) = \frac{A}{\sigma^2} \exp\left(-\frac{A^2}{2\sigma^2}\right) \tag{1.1}$$

where A (which is assumed to be positive) represents the envelope amplitude and σ^2 is the variance of the Gaussian distributed in-phase and quadrature components of the complex echo envelope [13].

1.2.2 K distribution

Jakeman and Pusey [7] introduced the use of the K distribution, a generalization of the Rayleigh distribution, in the context of microwave sea echo to model situations where the number of scatterers is not assumed to be large. The pdf is given by [14]

$$p_A(A) = \frac{2b}{\Gamma(\mu)}\left(\frac{bA}{2}\right)^{\mu} K_{\mu-1}(bA) \tag{1.2}$$

where $\Gamma(\bullet)$ is the Gamma function, $K_n(\bullet)$ is the modified Bessel function of the second kind, *n*-th order, and μ is a measure of the effective number of scatterers per resolution cell. In ultrasound, the resolution cell volume can be defined as the volume of the point spread function of the imaging system [15], i.e., the volume of the insonifed medium that contributes to any given point in the echo signal. In Equation (1.2), the *b* parameter can be expressed as

$$b = 2\sqrt{\frac{\mu}{E\left[A^2\right]}} \tag{1.3}$$

where $E[\bullet]$ is the expectation operator. The K distribution is a more general model that approaches the Rayleigh distribution in the limit $\mu \to \infty$ [14].

1.2.3 Homodyned K distribution

The homodyned K distribution was first introduced by Jakeman [16]. Besides incorporating the capability of the K distribution to model situations with low effective scatterer number densities, the homodyned K distribution can also model situations where a coherent signal component exists due to periodically located scatterers [11]. This makes the homodyned K distribution the most versatile of the three models discussed, but also the most complicated. The pdf of the homodyned K distribution does not have a closed-form expression; however, it can be expressed in terms of an improper integral as [14]

$$p_A(A) = A\int_0^\infty xJ_0(sx)\,J_0(Ax)\left(1+\frac{x^2\sigma^2}{2\mu}\right)^{-\mu} dx \tag{1.4}$$

where $J_0(\bullet)$ is the zeroth order Bessel function of the first kind, s^2 is the coherent signal energy, σ^2 is the diffuse signal energy, and μ is the same as in the K distribution. The derived parameter $k = s/\sigma$ is the ratio of the coherent to diffuse signal and can be used to describe the level of structure or periodicity in scatterer locations.

The pdf can also be expressed in terms of the Rice and Gamma distributions [10],

$$p_A(A) = \int_0^\infty p_R(A \mid z)\, p_\gamma(z)\, dz \tag{1.5}$$

Here $p_R(A \mid z)$ is the Rice distribution with scale parameter $\sigma\sqrt{z/\mu}$ and noncentrality parameter *s* whose pdf given by

$$p_R(A \mid z) = \frac{A\mu}{\sigma^2 z} \exp\left(-\frac{\mu\left(A^2 + s^2\right)}{2\sigma^2 z}\right) I_0\left(\frac{sA\mu}{\sigma^2 z}\right) \tag{1.6}$$

where $I_0(\bullet)$ is the zeroth order modified Bessel function of the first kind and $p_\gamma(z)$ is the Gamma distribution with shape parameter μ and scale parameter unity. The pdf of the Gamma distribution with these parameters is given by [10]

$$p_\gamma(z) = \frac{z^{\mu-1} e^{-z}}{\Gamma(\mu)} \tag{1.7}$$

The pdf of the homodyned K distribution can further be expressed as an infinite summation (using the form given by [17], expressing the pdf in terms of the parameters used in Equation (1.4), and simplifying),

$$p_A(A) = \sum_{n=0}^{\infty} \frac{\frac{2\mu A}{\sigma^2}}{\Gamma(\mu)(n!)^2} \left(\frac{\mu s A}{2\sigma^2}\right)^{2n} \left(\frac{1}{\sigma}\sqrt{\frac{\mu\left(s^2 + A^2\right)}{2}}\right)^{\mu-1-2n} K_{2n+1-\mu}\left(\frac{1}{\sigma}\sqrt{2\mu\left(s^2 + A^2\right)}\right) \tag{1.8}$$

The series is convergent except for the case when both $\mu < 1/2$ and $A = s$. The form given by Equation (1.8) is especially useful for numerically computing values of the pdf as it is usually possible to quickly obtain a good approximation of the pdf by considering only a small, finite number of terms in the infinite summation. The accuracy of the approximation depends on the particular parameter values for which the series is evaluated. In general, the rate of convergence is slower when the parameters are closer to the case where the series does not converge at all (i.e., $\mu < 1/2$ and $A = s$). Figure 1.1

shows four examples of the relative truncation error (the truncation error divided by actual pdf value) versus the number of terms considered in the truncated series.

To validate the approximation for a particular set of parameter values, the pdf can be sampled for values of A on the interval [0, a] where a is chosen to be sufficiently large such that $p_A(A)$ is negligible on the tail of the distribution (a, ∞]. Then, numerical integration can be performed on the sampled pdf. As the pdf should integrate to unity, if the result of numerical integration differs substantially from unity, the accuracy of the approximation is questionable, suggesting that more terms are needed to obtain a good approximation.

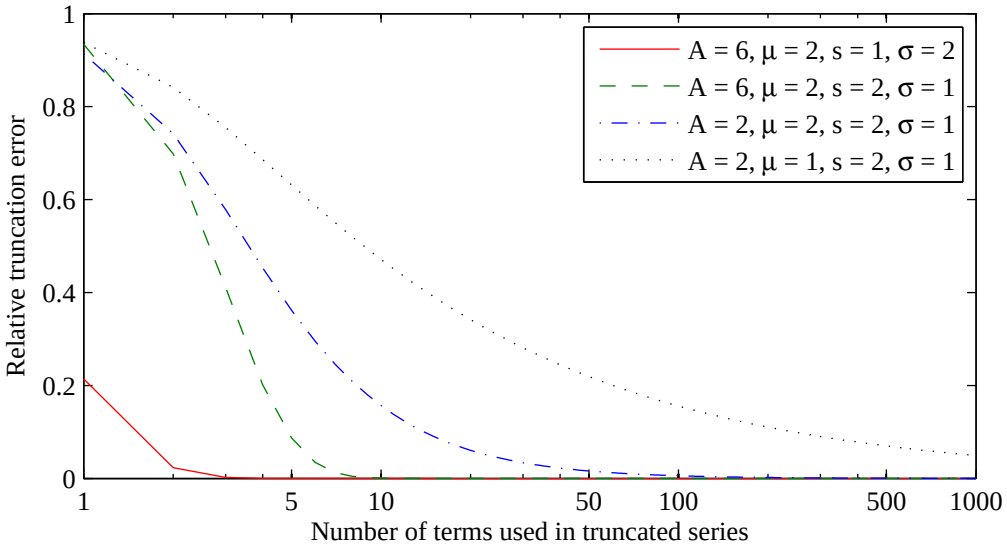

Figure 1.1. Relative truncation error versus the number of terms used in the truncated series given by Equation (1.8).

The homodyned K distribution model has been criticized (e.g., [18], [19], [20]) because of its analytical complexity. Hence, its use has been somewhat limited and other, more analytically tractable models such as the Nakagami distribution [18], [19], Weibull distribution [21], Rician inverse Gaussian distribution [20], and generalized gamma distribution [21] have been used instead. Because the homodyned K distribution is both

versatile and analytically complex, a goal of this work is to develop and apply methods to reduce the impact of this complexity while retaining the benefits of the versatility. By improving existing parameter estimation techniques, accurate parameter estimates can be obtained quickly. An improved parameter estimation algorithm will also provide more accurate information to better elucidate the relationships between the envelope statistics and the underlying structures responsible for the signals. Furthermore, as a by-product of the estimation algorithm, a geometrical interpretation into modeling of the envelope of backscattered ultrasound using the homodyned K distribution can be obtained.

The goals of this thesis are to develop a fast and accurate parameter estimation algorithm based on the homodyned K distribution, test the limits of the estimation algorithm, establish the spatial resolution of parameter imaging based on the quantifying the estimate errors, and apply the estimation algorithm to experimental data and animal models to evaluate the diagnostic potential of envelope-based statistics. The remainder of this thesis is organized as follows. In Chapter 2, existing parameter estimation methods are reviewed and evaluated and a new estimation algorithm is presented to address the shortcomings of the existing methods. Chapter 3 presents validation of the proposed estimation algorithm through the use of simulated and experimental data. The bias and variance of estimates versus spatial resolution and other factors affecting estimates are examined in Chapter 4. Suggestions for future work and concluding remarks are included in Chapter 5.

CHAPTER 2
PARAMETER ESTIMATION

2.1 Introduction

As a mathematical model, the homodyned K distribution is of practical use only when it can be used to model actual data. Parameter estimates, obtained by fitting the model to data, can in turn be used to describe underlying material properties. Ideally, a maximum likelihood estimator would be used; however, due to the analytical complexity of the homodyned K distribution, this approach is not feasible and alternative approaches must be explored instead.

2.1.1 Existing methods

Parameter estimation of the homodyned K distribution has received modest attention in the literature. The most frequently used methods involve the use of even moments (discussed in Section 2.1.1.1); however, a number of other approaches have also been proposed, some of which are discussed in Section 2.1.1.2.

2.1.1.1 Even moments

Dutt and Greenleaf [14] observed that the first few even moments of the homodyned K distribution have relatively simple closed-form expressions,

$$E\left[A^2\right] = s^2 + 2\sigma^2 \tag{2.1}$$

$$E\left[A^4\right] = 8\left(1+\frac{1}{\mu}\right)\sigma^4 + 8\sigma^2 s^2 + s^4 \tag{2.2}$$

$$E\left[A^6\right] = 48\left(1+\frac{3}{\mu}+\frac{2}{\mu^2}\right)\sigma^6 + 72\left(1+\frac{1}{\mu}\right)\sigma^4 s^2 + 18\sigma^2 s^4 + s^6 \tag{2.3}$$

Given N samples of the echo envelope, $a_i,\ i=1,2,\ldots,N$, moments of the envelope amplitude of order ν can be estimated as

$$\hat{E}\left[A^{\nu}\right]=\frac{1}{N}\sum_{n=1}^{N}a_n^{\nu} \tag{2.4}$$

By equating empirical estimates of the moments with the theoretical moments given by Equations (2.1)-(2.3), estimates of the parameters of the homodyned K distribution can be obtained. This method of parameter estimation is inadequate for several reasons. First, it requires solving a system of three nonlinear equations in three variables. While it is possible to solve the system analytically in closed form (see Appendix A), parameters obtained by solving the system of equations are not always valid (i.e., real and positive). Alternatively, it is possible to search for a set of parameters that minimizes some error criterion (such as mean squared error) between the theoretical and estimated moments using a gradient descent approach. Unfortunately, this approach is susceptible to convergence to local minima. While other search algorithms may not have this limitation, computational complexity can be a problem. Finally, note that the convenience of having simple closed form expressions for the moments comes at the expense of having to use high order moments. It may not be desirable to use high order moments (e.g., fourth and sixth moments) because their estimates can be more easily corrupted by large outliers compared to lower order moments.

2.1.1.2 Miscellaneous

Dutt [10] investigated several other estimation approaches, including using lower order integer moments (first, second, and third moments) and using signal-to-noise ratio (SNR) and skewness derived from these lower order moments. Unfortunately, these approaches all relied on approximations of the first, second, and third moments of the

homodyned K distribution. While these approximations allowed for efficient estimators to be implemented, the estimators were found to perform poorly in terms of consistency. Eltoft [22] developed an iterative parameter estimation algorithm based on an approximation of the pdf of the homodyned K distribution. Again, the use of an approximation limited the usefulness of such an approach.

Parameter estimation of the simpler K distribution has received significantly more attention in the literature. A number of parameter estimation approaches have been proposed, including the use of neural networks [23], [24]. The performance of estimators based on neural networks has been mixed and the computational complexity can be problematic. Nonetheless, such an approach could be adapted for use with the homodyned K distribution.

2.2 SNR, Skewness, and Kurtosis Method

2.2.1 Introduction, background, and motivation

Most parameter estimation algorithms for the homodyned K distribution somehow involve the use of moments; however, the choice of moment order has been investigated with varied results. Apparently due to the analytical convenience, Dutt [10] used even integer moments to estimate parameters of the homodyned K distribution. However, it has been reported that the use of fractional moment orders yields more robust estimates [25], [26] for the simpler, but related, K distribution. Prager et al. [27] found moment order 1.8 to be optimal for speckle discrimination using the homodyned K distribution; however, it has been reported that this claim may not be justifiable and that a simple optimum moment order for parameter estimation does not exist [28].

Based on the lack of consensus in the literature for what constitutes the optimal moment orders, it would be desirable to employ an estimation algorithm capable of using arbitrary moment orders. Then, the choice of moment order could be optimized for the particular estimation algorithm, or even the particular data set. The following sections describe the framework for an estimation algorithm that is both exact (i.e., does not resort to any algebraic approximations) and flexible (able to use arbitrary moment orders).

2.2.2 Nonparametric classifiers: SNR, skewness, and kurtosis

While the homodyned K distribution model is a function of three model parameters (μ, s, and σ), only two parameters yield independent information. Because the s and σ parameters scale together with the relative amplitude of the envelope, only their ratio, expressed as the amplitude independent parameter $k = s / \sigma$, is important. The estimation methods described in Section 2.1.1.1 require simultaneous estimation of all three model parameters. It may be desirable to estimate only the two independent model parameters k and μ. This is possible through the use of certain nonparametric classifier functions that describe data in a general way, free from any assumed models. That is, nonparametric classifiers are used as an intermediate step between the raw data and the parameter estimates (see Figure 2.1).

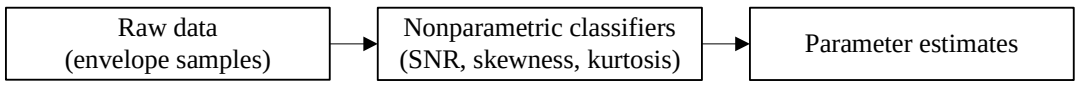

Figure 2.1. Procedure for parameter estimation using nonparametric classifiers.

Various nonparametric classifiers have been used in echo envelope signal processing. Dutt and Greenleaf [25] used SNR to estimate the scatterer number density

using the K distribution, Prager et al. [27] used SNR and skewness as discriminant functions for speckle, and Wachowiak et al. [23] used functions based on skewness and kurtosis as inputs to artificial neural networks to estimate parameters of the K distribution. As discussed in Section 2.1.1.2, Dutt investigated the use of SNR and skewness for parameter estimation of the homodyned K distribution. Wear et al. [29] used the square of the SNR to estimate the number of scatterers per resolution cell. Note, however, that the square of the SNR was found to be sensitive only in the range of small scatterer number densities, i.e., one or two scatterers per resolution cell [29]. Finally, it has been noted that skewness and kurtosis can be used to test whether or not a measured envelope follows the Rayleigh distribution [30].

Motivated by the use of these nonparametric classifiers in the literature, all three classifiers (SNR, skewness, and kurtosis) were used in the proposed estimation algorithm. To allow greater flexibility, these statistical classifiers are based on arbitrary powers of the envelope, following previous work [25], [31]. Algebraically, the SNR, skewness, and kurtosis of samples of the echo envelope raised to an arbitrary positive power ν can be expressed as [27], [32]

$$R_\nu = \frac{E[A^\nu]}{\left(E[A^{2\nu}] - E^2[A^\nu]\right)^{1/2}} \tag{2.5}$$

$$S_\nu = \frac{E[A^{3\nu}] - 3E[A^\nu]E[A^{2\nu}] + 2E^3[A^\nu]}{\left(E[A^{2\nu}] - E^2[A^\nu]\right)^{3/2}} \tag{2.6}$$

$$K_\nu = \frac{E[A^{4\nu}] - 4E[A^\nu]E[A^{3\nu}] + 6E[A^{2\nu}]E^2[A^\nu] - 3E^4[A^\nu]}{\left(E[A^{2\nu}] - E^2[A^\nu]\right)^2} \tag{2.7}$$

Note that the signal-to-noise ratio R_ν can also be recognized as the reciprocal of the coefficient of variation (CV). Also, the terms in the denominators of Equations (2.5)-

(2.7) can be recognized as powers of the variance of the envelope samples raised to an arbitrary positive power. As such, they are guaranteed to be positive, ensuring that these functions are well defined because division by zero does not occur for any valid combination of model parameters.

These classifier functions provide a good basis for characterizing the shape of the distribution of many kinds of data. The SNR measures the mean divided by the standard deviation, the skewness quantifies the asymmetry of the distribution, and the kurtosis characterizes the peakedness of the distribution. In particular, these classifiers can be used to describe the distribution of envelope samples. Figure 2.2 shows plots of pdf's of the homodyned K distribution illustrating the effects of shape of the distribution on the classifier function values, and Table 2.1 lists the parameters used to generate the pdf's. Each pdf was approximated numerically using a finite number of terms in Equation (1.8).

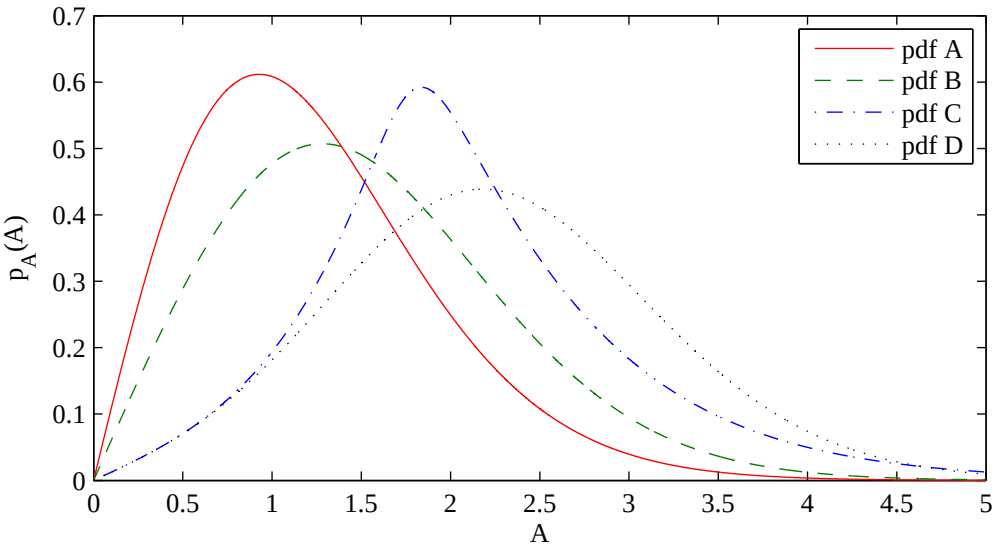

Figure 2.2. Plots of pdf's of the homodyned K distribution using various model parameters.

The SNR, skewness, and kurtosis were calculated using the methods described in Section 2.2.3. The SNR increases monotonically for these four pdf's as the peak (i.e., mode) moves to the right and hence the mean increases. Consistent with shapes of the

curves in Figure 2.2, pdf D has the lowest skewness while pdf's A and C have somewhat larger skewness values. Finally, the kurtosis of pdf's A, B, and D are all small compared to the kurtosis of pdf C which is clearly the most peaked.

Table 2.1. Parameters for pdf's plotted in Figure 2.2. The SNR, skewness, and kurtosis are based on moment order $\nu = 1$.

pdf	Model parameters						
	μ	s	σ	$k = s/\sigma$	SNR	skewness	kurtosis
A	10	0.1	1	0.1	1.81	0.83	3.83
B	10	1	1	1	1.95	0.64	3.40
C	1.2	1.8	1	1.8	2.34	1.03	5.51
D	10	2	1	2	2.49	0.31	3.08

2.2.3 Moments of arbitrary order of the homodyned K distribution

Because the estimation algorithm is to be based on arbitrary moment orders, some initial development is needed. Moments of arbitrary order ν of the homodyned K distribution can be expressed as [27]

$$E\left[A^{\nu}\right] = \int_0^{\infty} \left(\frac{2\sigma^2}{\mu}\right)^{\frac{\nu}{2}} \frac{\Gamma\left(1+\nu/2\right)}{\Gamma\left(\mu\right)} x^{\frac{\nu}{2}+\mu-1} e^{-x}\, {}_1F_1\left(\frac{-\nu}{2};1;\frac{-\mu s^2}{2\sigma^2 x}\right) dx \tag{2.8}$$

where ${}_1F_1\left(a;b;x\right)$ is the confluent hypergeometric function of the first kind. By substituting $k = s/\sigma$ in the argument of the hypergeometric function, defining the improper integral as a function of three variables,

$$I\left(k,\mu,\nu\right) = \int_0^{\infty} \frac{\Gamma\left(1+\nu/2\right)}{\Gamma\left(\mu\right)} x^{\frac{\nu}{2}+\mu-1} e^{-x}\, {}_1F_1\left(\frac{-\nu}{2};1;\frac{-\mu k^2}{2x}\right) dx \tag{2.9}$$

and pulling constants out of the integral, Equation (2.8) can be written as

$$E\left[A^{\nu}\right] = \left(\frac{2\sigma^2}{\mu}\right)^{\frac{\nu}{2}} I\left(k,\mu,\nu\right) \tag{2.10}$$

Performing the integration in Equation (2.9) and simplifying,

$$I\left(k,\mu,\nu\right)=\frac{\Gamma\left(1+\nu/2\right)}{\Gamma\left(\mu\right)}\left[\Gamma\left(\eta\right){}_1F_2\left(-\frac{\nu}{2};1,1-\eta;\frac{k^2\mu}{2}\right)-\right.$$
$$\left.\frac{\Gamma\left(\mu\right)\pi}{\Gamma\left(-\nu/2\right)\Gamma^2\left(1+\eta\right)\sin\left(\eta\pi\right)}\left(\frac{k^2\mu}{2}\right)^{\eta}{}_1F_2\left(\mu;1+\eta,1+\eta;\frac{k^2\mu}{2}\right)\right] \tag{2.11}$$

where ${}_1F_2\left(a;b,c;x\right)$ is a hypergeometric function and, for convenience, the definition

$$\eta=\mu+\frac{\nu}{2} \tag{2.12}$$

is used. Thus, moments of the homodyned K distribution of arbitrary order can be evaluated numerically in a relatively simple way using Equations (2.10) and (2.11).

Some discussion on the convergence of Equation (2.11) is warranted. When ν is an even integer, Equation (2.11) can be expressed in a much simpler form [10],

$$I\left(k,\mu,\nu\right)=\frac{\left(n!\right)^2}{\Gamma\left(\mu\right)}\sum_{m=0}^{\nu/2}\frac{\Gamma\left(\nu/2+\mu-m\right)}{\left(m!\right)^2\left(\nu/2-m\right)!}\left(\frac{k^2\mu}{2}\right)^m \tag{2.13}$$

When applicable, use of Equation (2.13) instead of Equation (2.11) is preferable because the former also eliminates the difficulties in dealing with the term $\Gamma\left(-\nu/2\right)$ in Equation (2.11), which is infinite when ν is an even integer. Hypergeometric functions of the form ${}_pF_q\left(a_1,a_2,...,a_p;b_1,b_2,...,b_q;x\right)$ are convergent for all x when $p\le q$ provided that none of the b_i, $i=1,2,...,q$ are negative integers or zero [33]. Therefore, when η is an integer, the hypergeometric function in the first term of Equation (2.11) diverges. The second term in Equation (2.11) also diverges when η is an integer because of the term $\sin\left(\eta\pi\right)=0$ that appears in the denominator. Should it be desired to compute moment orders where η is an integer and ν is not an even integer, linear interpolation can be used by considering small perturbations around the offending parameters, either in the form

$$I\left(k,\mu,\nu\right)\approx\frac{I\left(k,\mu+\varepsilon,\nu\right)+I\left(k,\mu-\varepsilon,\nu\right)}{2} \tag{2.14}$$

or

$$I(k,\mu,\nu) \approx \frac{I(k,\mu,\nu+\varepsilon)+I(k,\mu,\nu-\varepsilon)}{2} \tag{2.15}$$

where ε is a small real number. The error in these approximations can be made arbitrarily small by choosing a sufficiently small ε.

2.2.4 Nonparametric classifiers using arbitrary moment orders

The theoretical value for the SNR of envelope samples raised to arbitrary positive power ν can be expressed in terms of parameters of the homodyned K distribution by substituting Equation (2.10) into Equation (2.5),

$$R_\nu = \frac{\left(2\sigma^2/\mu\right)^{\frac{\nu}{2}} I(k,\mu,\nu)}{\left[\left(2\sigma^2/\mu\right)^{\nu} I(k,\mu,2\nu) - \left(\left(2\sigma^2/\mu\right)^{\frac{\nu}{2}} I(k,\mu,\nu)\right)^2\right]^{1/2}} \tag{2.16}$$

which simplifies to

$$R_\nu = \frac{I(k,\mu,\nu)}{\sqrt{I(k,\mu,2\nu) - I^2(k,\mu,\nu)}} \tag{2.17}$$

Note that Equation (2.17) is a function of the two independent model parameters as claimed in Section 2.2.2. This property also holds for S_ν and K_ν by using Equations (2.6), (2.7), and (2.10), giving

$$S_\nu = \frac{I(k,\mu,3\nu) - 3I(k,\mu,\nu)I(k,\mu,2\nu) + 2I^3(k,\mu,\nu)}{\left(I(k,\mu,2\nu) - I^2(k,\mu,\nu)\right)^{3/2}} \tag{2.18}$$

and

$$K_\nu = \frac{I(k,\mu,4\nu) - 4I(k,\mu,\nu)I(k,\mu,3\nu) + 6I(k,\mu,2\nu)I^2(k,\mu,\nu) + 3I^4(k,\mu,\nu)}{\left(I(k,\mu,2\nu) - I^2(k,\mu,\nu)\right)^2} \tag{2.19}$$

In fact, the property holds for any finite functional combination of classifier functions F in the form

$$F = \frac{\left(\sum_{n=1}^{N} a_n \prod_{l=1}^{L} E^{x_{l,n}} \left[A^{w_{l,n}} \right] \right)^{\alpha}}{\left(\sum_{m=1}^{N} b_m \prod_{p=1}^{L} E^{z_{p,m}} \left[A^{y_{p,m}} \right] \right)^{\beta}} \tag{2.20}$$

provided that the criterion

$$\alpha \sum_{l=1}^{L} w_{l,n} x_{l,n} = \beta \sum_{p=1}^{L} y_{p,m} z_{p,m} \tag{2.21}$$

is satisfied for all pairs of $m, n \in 1, 2, ..., N$ where α, β, a_n, b_m, $w_{l,n}$, $x_{l,n}$, $y_{p,m}$, and $z_{p,m}$ are real constants and L and N are positive, real constants. Equations (2.5)-(2.7) are specific realizations of the general form given by Equation (2.20).

2.2.5 Estimation using level sets

Martin-Fernandez et al. [31] first introduced an estimation methodology for the homodyned K distribution using level sets; however, the algorithm was based on only the SNR. The present estimation algorithm contains several incremental improvements over this initial idea, most notably the extension to include skewness and kurtosis.

Fundamentally, parameter estimates are obtained by following the procedure outlined in Figure 2.1 and equating theoretical values for the nonparametric classifiers (given by Equations (2.17)-(2.19)) with empirical values estimated from envelope samples. The complexity of these equations rules out any closed-form algebraic solution, but other approaches can be used instead.

For a fixed moment order, ν, the nonparametric classifiers are functions of two variables. Therefore, given an estimate of a nonparametric classifier, it is possible to map out a curve of possible parameter values (a level curve) in two dimensions. Such an example is shown in subplot (a) in Figure 2.3. By considering a second classifier

function, a second level curve can be drawn (subplot (b) in Figure 2.3). Because there are two unknown model parameters, two classifier functions should uniquely identify a parameter estimate because their level curves should intersect at one point. However, for improved robustness, three classifier functions are used (subplot (c) in Figure 2.3) resulting in an overdetermined system. Furthermore, level curves using a number of different moment orders can be used, resulting in a further overdetermined system.

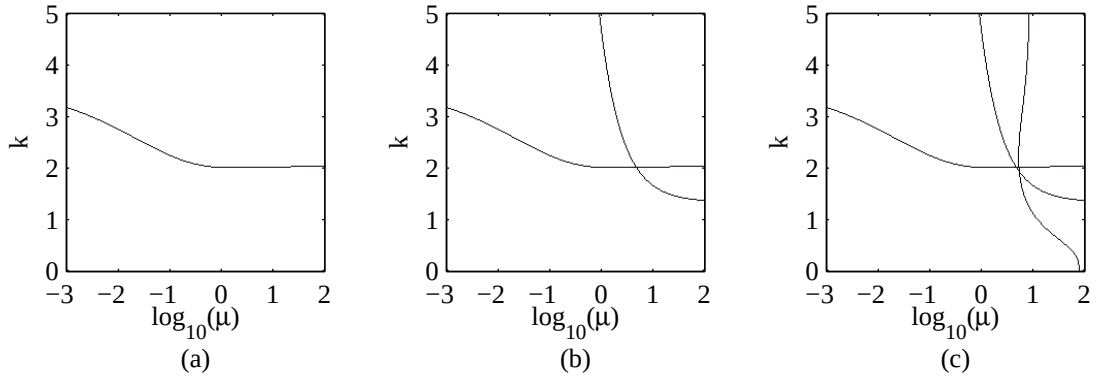

Figure 2.3. Examples of level curves using moment order $\nu = 1$ for (a) SNR, (b) SNR and skewness, and (c) SNR, skewness, and kurtosis. Intended parameter values: $k = 2$ and $\log_{10}(\mu) = 0.7$.

2.2.6 Implementation issues

2.2.6.1 Sampling nonparametric classifier functions

To limit the amount of computation needed to perform parameter estimation, theoretical values of the nonparametric classifiers given by Equations (2.17)-(2.19) are first sampled on a rectangular grid. Provided that this sampling is sufficiently dense, good approximations of level curves can be constructed solely from the samples of the nonparametric classifiers without resorting to tedious and time-consuming calculations. Thus, the sampling only needs to be performed once, and thereafter the sampled theoretical classifier function values can be used repeatedly for parameter estimation.

To encompass the expected range of parameter values obtained from simulations, phantoms, and experimental data, a 501×501 point grid was used with k on the interval $[0,\ 5]$ and μ on the interval $[0.001,\ 100]$. The k parameter was sampled on a linear scale while the μ parameter was sampled on a logarithmic scale. Therefore, the spacing between the values of k was 0.01 and the spacing between the values of $\log_{10}(\mu)$ was 0.01.

2.2.6.2 Determining level sets

Each level curve is determined by finding a set of contiguous points on the sampling grid such that the theoretical classifier function value at each point closely approximates the estimated classifier function value. A sampled classifier function of a particular moment order can be denoted as a function of two variables as $F(k,\mu)$. Each complete level curve is determined using a two-stage process. First, for each value of μ used in the sampling process, the k values of all zero crossings of $F(k,\mu)-\hat{F}$ are found where $\hat{F}$ is the estimated classifier function value. Then, for each value of k used in the sampling process, the μ values of all zero crossings of $F(k,\mu)-\hat{F}$ are found. The collection of all the points where the zero crossings occur defines the level curve. Performing both of these steps ensures that a complete, connected level curve is found, as shown in the example in Figure 2.4. Note that the zero crossings typically occur between two points; the point closer to the zero crossing is chosen to make up the level curve (this is also illustrated in Figure 2.4).

2.2.6.3 Determining parameter estimates

Parameter estimates are obtained by considering the distance from each level curve to a point in (k, μ) space. The point where the L2-norm (i.e., the square root of the

sum of the squares of the distances) is minimized identifies the pair of parameter estimates. Note that this distance is measured with the k parameter on a linear scale and the μ parameter on a logarithmic scale. Figure 2.5 shows an example of this distance metric where the L2-norm was exhaustively calculated for each point on the sampling grid.

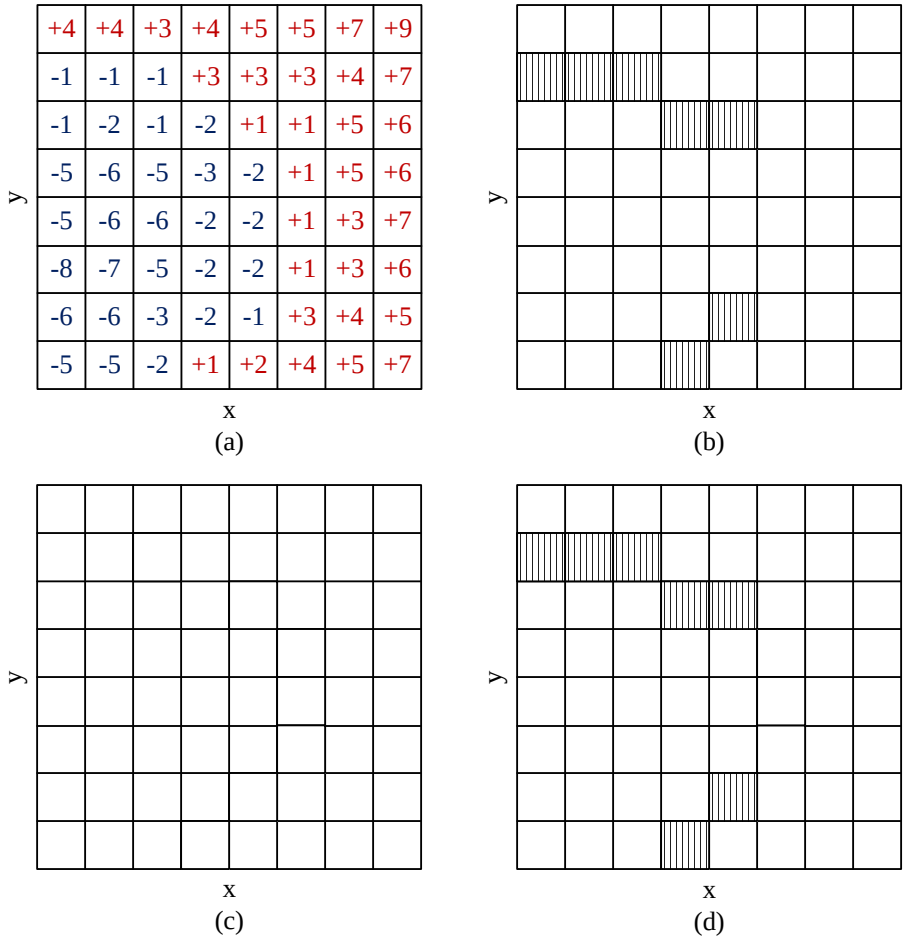

Figure 2.4. Example of the process of finding level curves: (a) the difference between the sampled classifier function and its estimated value, (b) the points on the level curve determined by the sign changes in y for constant x, (c) the points on the level curve determined by the sign changes in x for constant y, and (d) the complete level curve (the shading indicates whether each point was obtained from (b) or (c) or both).

Motivated by the example in subplot (b) of Figure 2.5, the point that minimizes the L2-norm could be determined by exhaustively calculating the L2-norm at each point on the grid where the classifier functions were evaluated, and simply selecting the minimum. While this is a reliable technique, it is time consuming. The example shown in

subplots (b) and (c) of Figure 2.5 suggests that the L2-norm using this estimation algorithm is a fairly well-behaved function, i.e., it does not have local minima scattered over the entire search space. Therefore, a more efficient search technique can be used to find the global minimum of the L2-norm.

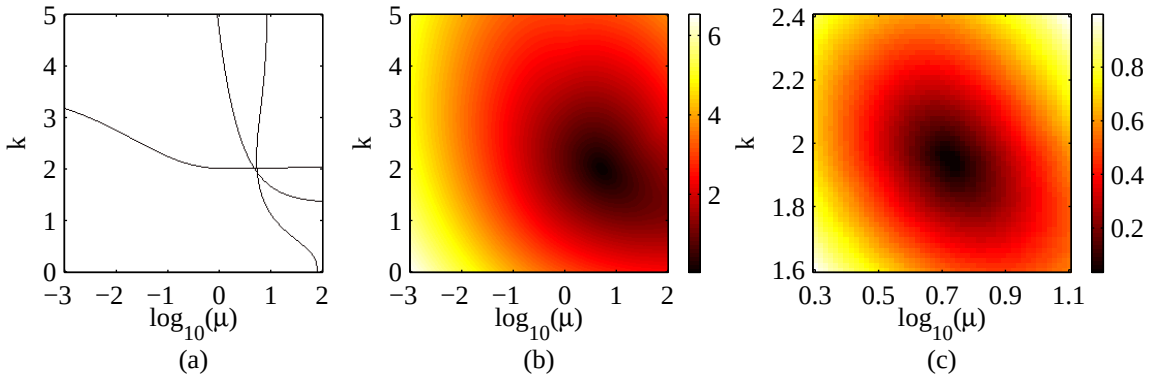

Figure 2.5. Illustrations of level curve distance metric: (a) SNR, skewness, and kurtosis level curves using moment order $\nu = 1$, (b) L2-norm of Euclidean distances from the three level curves, and (c) close-up view of L2-norm of Euclidean distances near the optimum. Intended parameter values: $k = 2$ and $\log_{10}(\mu) = 0.7$.

A grid search was implemented to locate the global minimum of the L2-norm. As implemented, the L2-norm is first coarsely sampled on a grid of 11×11 discrete points spanning the entire search space. The point where the L2-norm is minimized is selected as the center of a new search space that is one fourth the size of the original search space. This smaller search space is resampled on an 11×11 point grid, and the procedure is repeated until convergence is reached. This process is illustrated in Figure 2.6.

The grid search algorithm was validated against the exhaustive search by generating sets of samples of the homodyned K distribution using the approach described in Section 3.1.1. The k parameter values were drawn from the set {0.5, 1.0, …, 4.5} and the values of $\log_{10}(\mu)$ from the set {-2.5, -2.0, …, 1.5}. For each combination of model parameters, 10 independent sets of samples were generated. Estimates were performed on each set of samples using an exhaustive search and using a grid search. In every case, the

grid search located the same global minimum as the exhaustive search, suggesting that the grid search is sufficiently robust. Furthermore, the grid search algorithm was found to be roughly 160 times faster than the exhaustive search.

A gradient descent algorithm was also investigated. Although it was slightly faster than the grid search, it was found to be unacceptable for parameter estimation due to convergence to local minima.

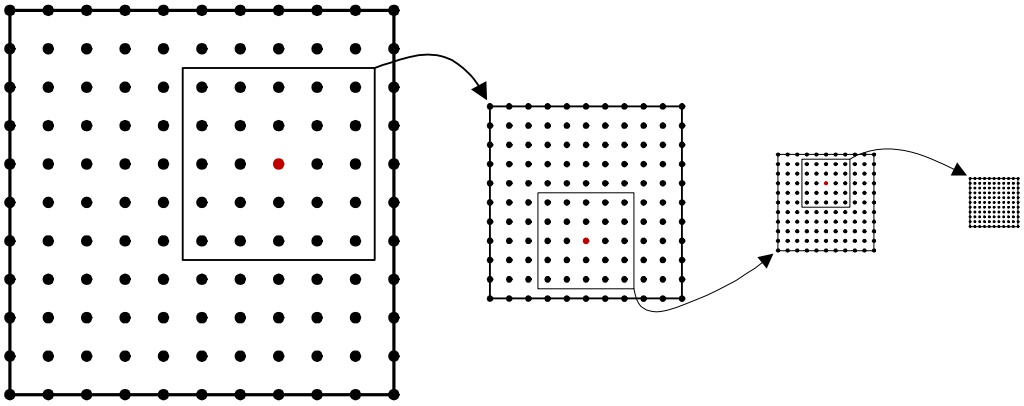

Figure 2.6. Illustration of four iterations of the grid search algorithm.

Note that the L2-norm at the optimum may give some indication of goodness of fit: if the L2-norm is small, the level curves come close to intersecting at a single point, if the L2-norm is large, they do not. A large L2-norm may suggest that the signal is noisy or that the assumptions used in deriving the homodyned K distribution model are violated.

2.2.7 Geometrical interpretation of level sets

By examining the collection of level sets, a geometrical interpretation of the estimation process can be obtained. For simplicity, Figure 2.7 shows examples of the intersection of only two level curves. In subplot (a), where the level curves intersect almost perpendicularly, parameter estimation is expected to be robust. In subplot (b), the curves are somewhat less perpendicular, but in subplot (c), they are almost parallel. In this case, any small perturbations in the estimates of the classifier functions used to

determine the level curves will shift the level curves a small amount. This small shift may cause the intersection point, and hence the parameter estimates, to change substantially. That is, nearly parallel lines represent an ill-conditioned system while nearly perpendicular lines represent a well-conditioned system [34]. For these reasons, parameter estimation is expected to be weaker for cases similar to the example in Figure 2.7(c).

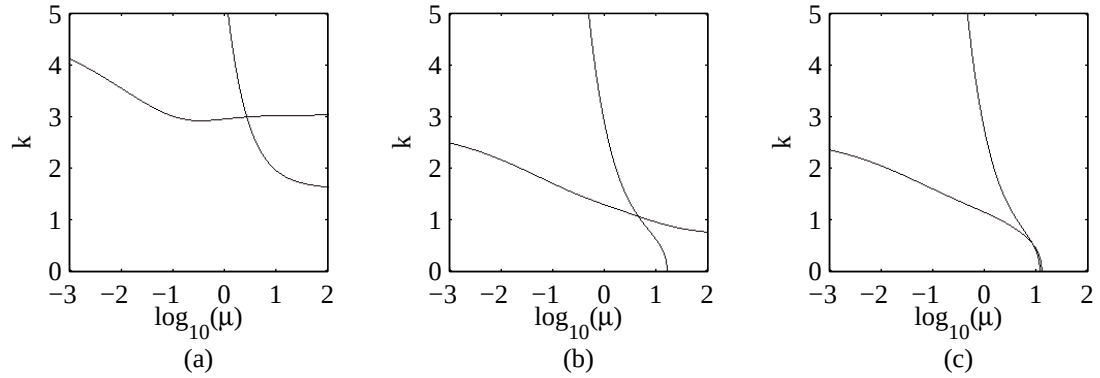

Figure 2.7. Three examples, each of two intersecting level curves (derived from SNR and skewness using moment order $\nu = 1$). Intended parameter values: (a) $k = 3$ and $\log_{10}(\mu) = 0.48$, (b) $k = 1$ and $\log_{10}(\mu) = 0.7$, and (c) $k = 0.5$ and $\log_{10}(\mu) = 1$.

One could attempt to address this problem by using many different level curves by considering different moments. While this would increase the complexity, it would not address the fundamental ill-conditioning of the inverse problem of parameter estimation because, for certain combinations of model parameters, the generated curves will have little variation in the parallel orientation between lines at the point of intersection regardless of the choice of moment order.

2.2.8 Interpretations of sampled classifier function data

Examination of the samples of the classifier functions reveals further insights into parameter estimation from the homodyned K distribution. Figure 2.8 shows the SNR, skewness, and kurtosis as functions of k and μ using moment order $\nu = 1$.

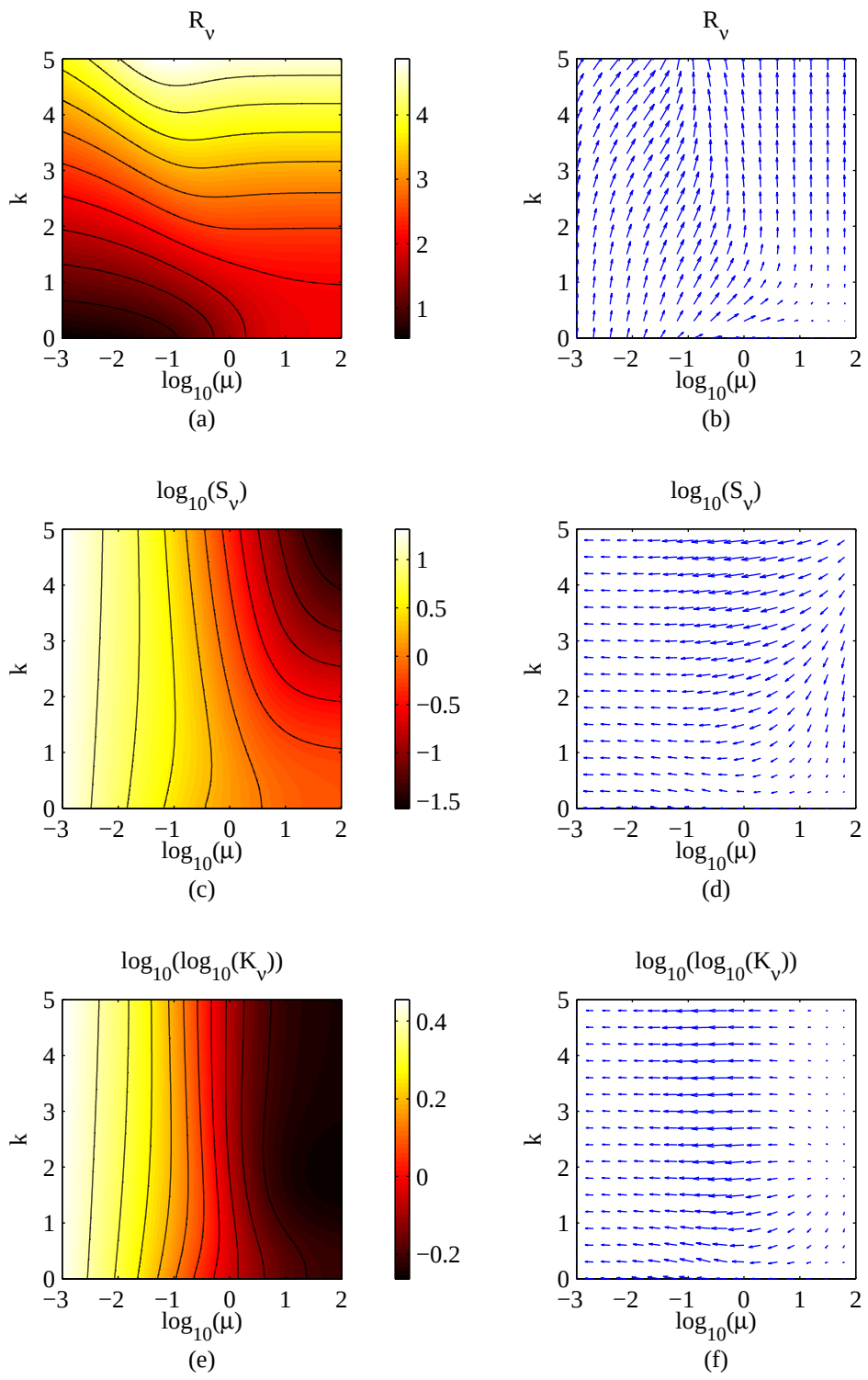

Figure 2.8. SNR, skewness, and kurtosis classifier functions for moment order $\nu = 1$. The left panels show level sets superimposed on top of the actual function values. The arrows in the right panels represent the direction and relative magnitude of the gradient. Logarithmic scaling is used for parameters with large dynamic range.

The gradient subplots, (b), (d), and (f) in Figure 2.8 help reveal where one would expect parameter estimation to work well and where one would expect parameter estimation to perform poorly when the SNR, skewness, and kurtosis classifier functions are used. In particular, observe that the gradient is very small for all three functions when μ is large and k is small.

The level curves in subplots (a), (c), and (e) of Figure 2.8 are consistent with the results in Table 2.1. The level curves are generally horizontal in subplot (a) because the SNR parameter increases as the k parameter increases. The level curves in subplot (e) are generally vertical because the kurtosis decreases as the μ parameter increases.

To verify that it is the homodyned K distribution model itself, and not some effect of the classifier functions, causing the gradient to be small for large μ and small k, pdf's of the homodyned K distribution were plotted (see Figure 2.9).

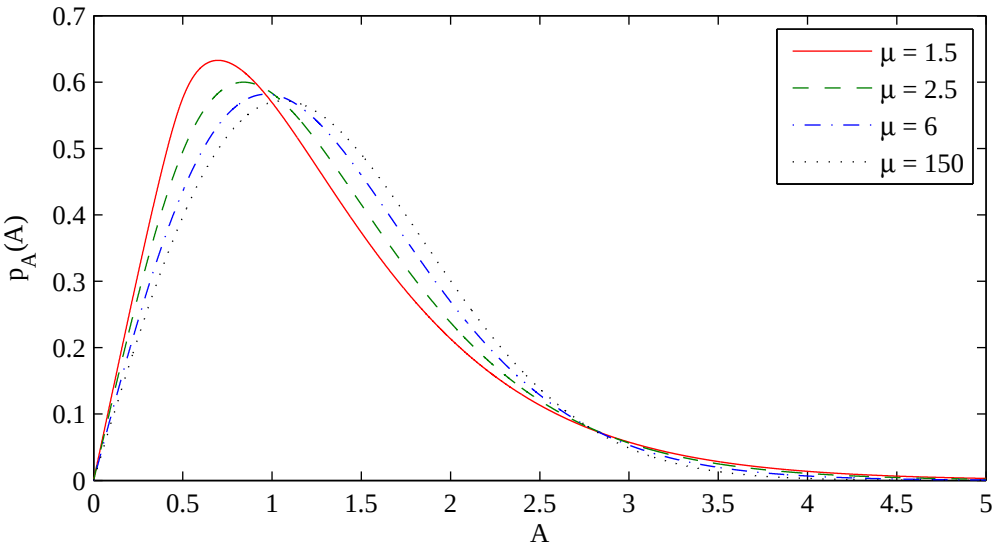

Figure 2.9. Variation in the pdf of the homodyned K distribution for different values of μ. For all four pdf's shown, parameters $s = 0.5$ and $\sigma = 1$ were used.

Visually, the differences between the pdf's for $\mu = 2.5$ and $\mu = 6$ are more substantial than the differences between the pdf's for $\mu = 6$ and $\mu = 150$. This illustrates the well-

known Rayleigh limit of about 10 scatterers per resolution cell, i.e., the point at which the envelope statistics are considered to be Rayleigh distributed [35], [36].

2.3 Choice of Moment Orders

Examination of the classifier functions based on different moment orders reveals functions that are qualitatively very different. For example, Figure 2.10 shows the SNR for two different moment orders. There exist substantial differences in orientation of the level curves for small values of μ. Due to these differences, it would be expected that parameter estimates obtained using different moment orders would have varying quality (i.e., bias and variation).

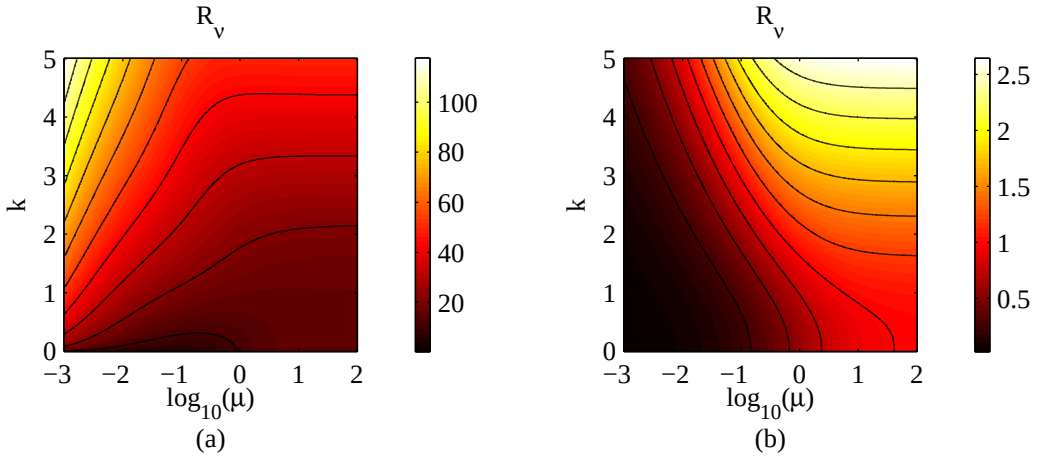

Figure 2.10. SNR as a function of k and μ for (a) $\nu = 0.1$ and (b) $\nu = 2$.

Based on the reasoning in Section 2.2.7, in order to obtain the best possible parameter estimates when using two level curves, it would be desirable to have level curves that intersect as close as possible to perpendicularly. When more than two level curves are used to estimate parameters, the sum of the angles between all pairs of level curves may be a more appropriate quantity to seek to maximize. Figure 2.11 shows three examples of this metric, each using four level curves. Note that while there are level curves in both subplots (b) and (c) that are perpendicular, the system in subplot (c) is

better conditioned. Also, the level curves in subplot (a) represent a relatively poorly conditioned system. These observations are reflected by the sum-of-all-angles metric.

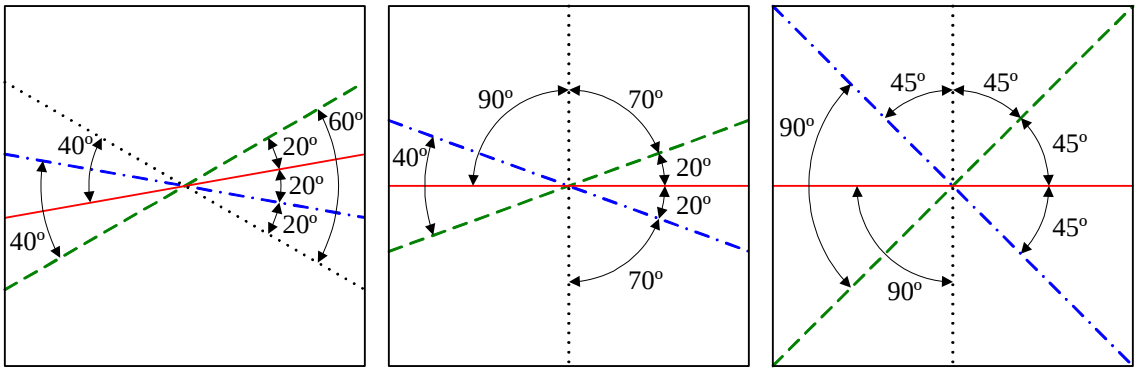

Figure 2.11. Three examples illustrating the angles between level curves. The sum of the angles between all pairs of level curves is (a) 200º, (b) 310º, and (c) 360º.

In order to optimize the sum of the angles between level curves, these angles must first be determined. To measure the angle between two level curves, it is useful to first define the angle of each curve with respect to a fixed reference. Given a classifier function $F(k,\mu)$ based on a particular moment order, the angle of the level curve at the point (k_1, μ_1) with respect to horizontal (i.e., the line given by constant k) is given by

$$\theta = \arctan\left(-\frac{\partial F / \partial \mu\big|_{k_1,\mu_1}}{\partial F / \partial k\big|_{k_1,\mu_1}} \right) \tag{2.22}$$

Note that $\partial F / \partial \mu$ and $\partial F / \partial k$ are components of the gradient of F; Equation (2.22) makes use of the property that the gradient and level curves are perpendicular to each other. The angle between two level curves can easily be found by applying Equation (2.22) to each level curve and taking the difference between the angles.

Using Equations (2.17)-(2.19), (2.11), and (2.22), the angles between level curves derived from SNR, skewness, and kurtosis could be derived as functions of k, μ, and ν in closed form. Then, calculus could be used to determine the derivative with respect to ν of the expression for the angles between level curves. By setting the derivative to zero and

solving for ν, the value of ν that results in the largest angle between level curves could be found. Unfortunately, this approach quickly becomes untenable because of the analytical complexity. However, a close approximation of this calculation can be made by working with the discrete samples of the classifier functions of various moment orders.

To implement this approximation, the SNR, skewness, and kurtosis functions were sampled on a grid as in Section 2.2.6.1: μ ranging from 0.001 to 100 (on a logarithmic scale) and k ranging from 0.0 to 5.0. Moment orders ranging from 0.02 to 1.0 in increments of 0.02 were used. Then, the SNR, skewness, and kurtosis functions for two moment orders at a time were considered. At each point on the sampling grid, the sum of the angles between all pairs of the six level curves (SNR, skewness, and kurtosis for each of the two moment orders considered) was found. Then the average value of this sum for all points on the sampling grid was determined. This calculation was repeated for all possible pairs of two moment orders, and the pair that maximized this sum was selected as the optimal moment orders. The optimal pair of moments was found to be $\nu = \{0.72, 0.88\}$, as shown in Figure 2.12. These two moments are used for parameter estimation throughout the rest of this work. The sum of angles between all pairs of level curves for this pair of moments is shown in Figure 2.13. These two moments are relatively small compared to the second, fourth, and sixth moments used in the even moments estimation algorithm described in Section 2.1.1.1, suggesting that this estimator is less sensitive to outliers. Note, however, that the calculation of kurtosis involves the use of the moment order 4ν. Thus, in some sense, moment orders as large as 3.52 are employed.

The choice of moment orders could be improved somewhat if there were information available about the a priori distribution of parameter values. The optimization used here assumes all parameter values on the sampling grid occur with equal probability; that is, it minimizes the total cost over the entire space of parameters k and μ examined. For particular pairs of model parameters (k, μ), other pairs of moment orders ν may yield better results.

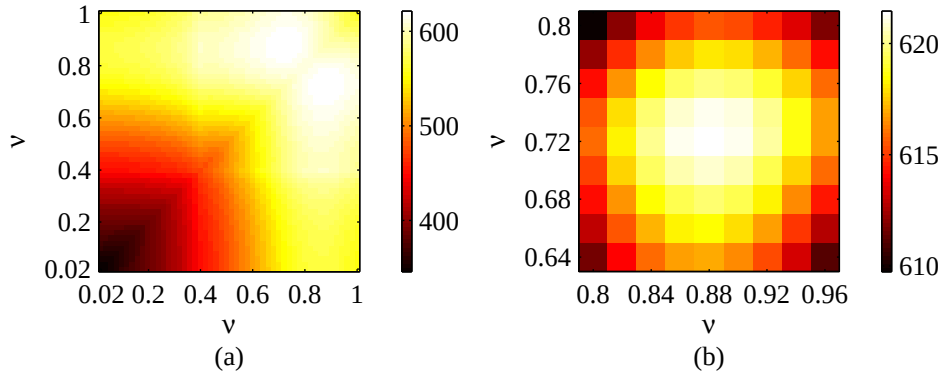

Figure 2.12. Average over all sampling points of the sum of angles between all pairs of level curves for classifier functions derived from two different moment orders. Subplot (b) shows a close-up view of the optimal pair of moment orders.

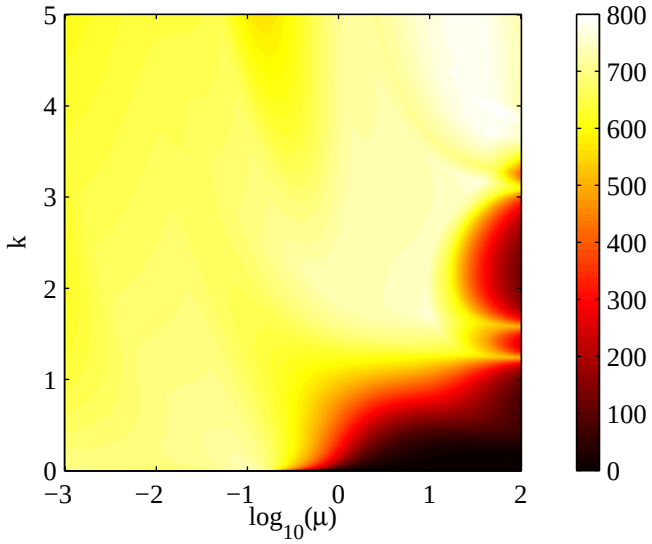

Figure 2.13. The sum of all angles between pairs of level curves for SNR, skewness, and kurtosis versus the two model parameters for moment orders 0.72 and 0.88.

2.4 Limitations

2.4.1 Model limitations

It deserves to be repeated that when the number of scatterers per resolution cell is large (i.e., greater than about 10), the statistics of the echo envelope approach the Rayleigh distribution, and hence little information about the scatterer number density can be obtained [37]. Therefore, reliable estimation is restricted to cases where the scatterer number density is sufficiently low.

Note that the estimation algorithm presented here is theoretically capable of measuring scatterer number densities up to 100. It would be reasonable to assume that any estimates above 10 are suspect. Therefore, when performing estimation on sets of data, postprocessing may need to be applied (e.g., rejection of samples with estimated densities above some threshold).

2.4.2 Estimator limitations

The most obvious limitation of the SNR, skewness, and kurtosis method as presented here is that the model parameters must fall within the range of the sampling grid used to compute the SNR, skewness, and kurtosis functions. It is impossible to make a parameter estimate when a level curve cannot be found in the sampled data. A more subtle limitation is that parameter estimation near the edges of the grid may be poor because the algorithm does not make use of what happens outside the sampling grid; the distance metric that the estimator seeks to minimize could be incorrect because it lacks the complete level curve. A contrived example illustrating this potential limitation with two level curves is shown in Figure 2.14. Lastly, note that signals acquired from closely separated scan lines are correlated [38], [39]. Under this condition of correlated samples,

the estimates of the moments of the samples (Equation (2.4)) are unbiased, but the estimates of SNR, skewness, and kurtosis may be biased [25], [30]. However, this has not been found to be a substantial problem in practice.

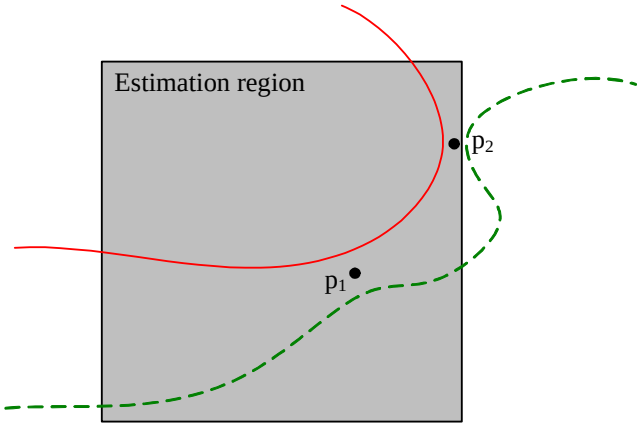

Figure 2.14. Example illustrating the potential poor estimator performance near the edges of the sampling grid. The estimation region (shaded) represents the range of sampled classifier function values and the lines represent two level curves. The point that minimizes the L2-norm of the distance from the two level curves is p_2, but the estimator will find p_1 which minimizes the L2-norm using only the information available inside the estimation region.

CHAPTER 3
TESTING AND VALIDATION

The estimation algorithm presented in Chapter 2 was tested in a variety ways that were increasingly representative of the ultimate goal of the statistical modeling of the envelope: being able to discriminate different tissue types associated with disease. Specifically, the testing methods applied artificially generated samples of known distribution, computer simulations, physical phantoms, biological phantoms, and animal tumor models.

3.1 Direct Method

The simplest method of testing the estimation routine is by making parameter estimates from sets of samples of the homodyned K distribution generated with known parameters. This same type of approach has been used to evaluate different estimators for the Nakagami distribution [40]. This method provides a fast and efficient way to evaluate the estimation algorithm, make comparisons with other estimation techniques, and evaluate factors that may affect estimate bias and variation.

3.1.1 Generating samples of the homodyned K distribution

Independent, identically distributed (i.i.d.) samples of the homodyned K distribution can be generated by exploiting the form given by Equations (1.5)-(1.7) and using the approach in [31]. That is, i.i.d. samples of the homodyned K distribution with parameters μ, s, and σ can be created by first generating samples of the gamma distribution with shape parameter μ and scale parameter unity. These samples of the

gamma distribution can be denoted as z_i, $i = 1, 2, ..., n$, where n is the number of samples to be generated. For each sample z_i, the i.i.d. samples of the homodyned K distribution are computed by generating a sample of the Rice distribution with scale parameter $\sigma\sqrt{z_i / \mu}$ and noncentrality parameter s. Using properties of the Rice distribution [41], these samples of the Rice distribution are given by

$$A_i = \sqrt{x_i^2 + y_i^2} \tag{3.1}$$

where x and y are independent samples of the Gaussian distribution with mean values of s and zero, respectively, and each with variance $\sigma\sqrt{z_i / \mu}$, i.e.,

$$x_i = s + X_i \sigma\sqrt{z_i / \mu} \tag{3.2}$$

$$y_i = Y_i \sigma\sqrt{z_i / \mu} \tag{3.3}$$

where X_i and Y_i are i.i.d. samples of the unit Gaussian distribution.

In summary, i.i.d. samples of the homodyned K distribution can be generated using samples of simpler distributions, viz., the gamma and Gaussian distributions. An illustration summarizing the procedure for transforming these samples of the gamma and Gaussian distributions into a sample of the homodyned K distribution is shown in Figure 3.1.

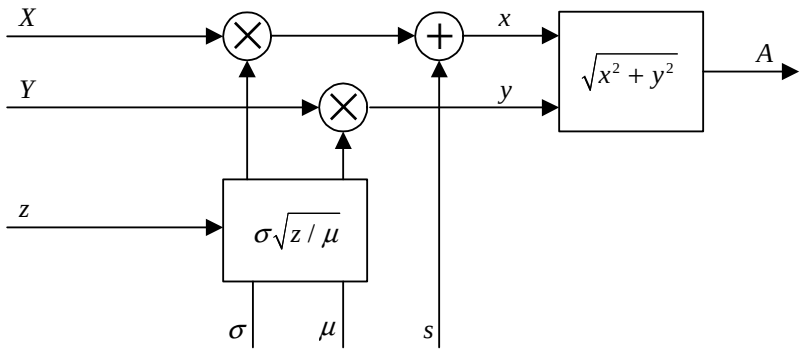

Figure 3.1. Illustration of the procedure for generating a sample A of the homodyned K distribution. Inputs σ, μ, and s are the desired parameters of the homodyned K distribution, X and Y are i.i.d. samples of the unit Gaussian distribution, and z is a sample of the gamma distribution.

Samples of the simpler gamma and Gaussian distributions can be generated using built-in functions in common software applications including MATLAB (The MathWorks, Inc., Natick, MA), Mathematica (Wolfram Research, Inc., Champaign, IL), and Microsoft Excel (Microsoft Corporation, Redmond, WA).

3.1.2 Comparison of estimation methods

The SNR, skewness, and kurtosis method (Section 2.2) was compared with the even moments method (Section 2.1.1.1) by applying each estimator to i.i.d. samples generated for a variety of parameter values and sample sizes. For each combination of parameter values and sample size examined, 100 independent estimation trials were performed to establish the variability of estimates between trials. To implement the even moments method, a gradient descent algorithm was used to find the set of model parameters that minimized the sum of the squares of the relative error in the even moments,

$$\varepsilon = \sum_{n=1}^{3} \left(\frac{E\left[A^{2n}\right] - \hat{E}\left[A^{2n}\right]}{E\left[A^{2n}\right]} \right)^2 \tag{3.4}$$

The relative error, rather than absolute error, was used because the absolute error is generally much larger for the sixth moment than for the second moment. To help mitigate the main limitation of the gradient descent approach, i.e., convergence to local minima, the gradient descent search was started from the intended model parameters which had been used to generate the i.i.d. data. Furthermore, because estimates obtained using the SNR, skewness, and kurtosis method are intrinsically limited to a certain range of parameters while estimates from the even moments method are not, any estimates from the even moments method that fell outside of the range used by the SNR, skewness, and

kurtosis method were discarded. Finally, for the cases when the SNR, skewness, and kurtosis method failed to produce an estimate (because the nonparametric classifiers were out of range), the corresponding even moments estimate was not considered.

The bias and standard deviation (SD) of the parameter estimates obtained from each estimation algorithm were calculated for each set of samples. The bias and SD were normalized by the true parameter values to allow comparison between estimates obtained for different parameter values and between the two estimation algorithms:

$$\text{relative bias} = \frac{E\left[\hat{x}\right] - x}{x} \tag{3.5}$$

$$\text{normalized SD} = \frac{\sqrt{\text{Var}\left[\hat{x}\right]}}{x} \tag{3.6}$$

where x represents the true parameter value (used to generate the i.i.d. samples), $\hat{x}$ represents the estimates of the parameter value from the 100 independent trials, and $\text{Var}[\bullet]$ is the sample variance. A representative sample of the results is shown in Figure 3.2. For the majority of parameter values tested, the SNR, skewness, and kurtosis method yielded estimates with lower bias and SD than the even moments method despite the untenable advantages used with the even moments method in this comparison. Furthermore, the speeds of the two estimation algorithms are roughly equal. By pushing the complexity back into the nonparametric classifier function calculation, the SNR, skewness, and kurtosis method is fast and produces more accurate and precise estimates.

3.2 Simulations

Computer simulations were performed using the Field II ultrasound simulation program [42], [43] to examine the effects of varying scatterer number densities and organizational patterns on the statistics of the envelope.

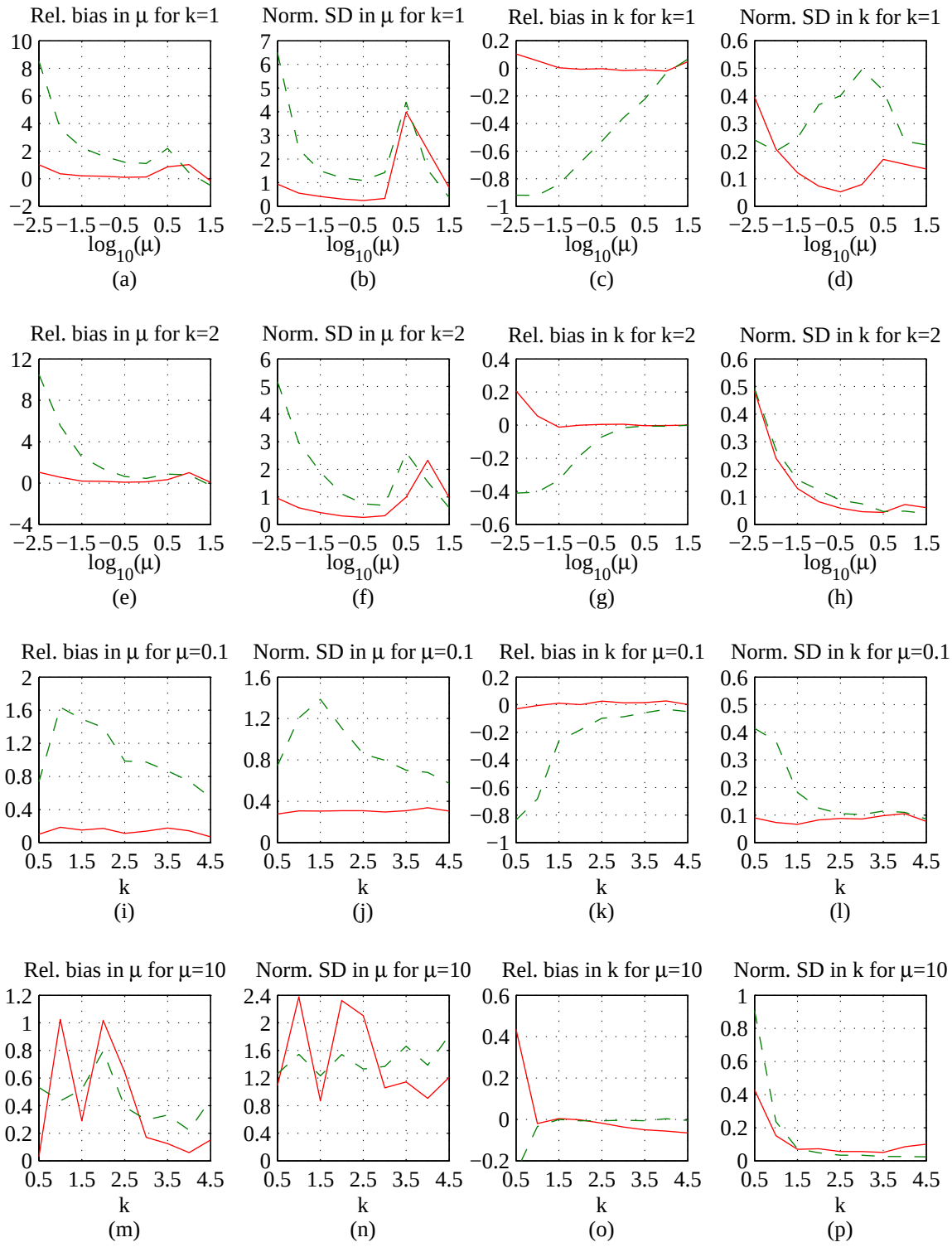

Figure 3.2. Relative bias and normalized SD of estimates derived using the SNR, skewness, and kurtosis method (solid red lines) and the even moments method (dashed green lines) as functions of the μ parameter with k fixed (subplots (a)-(h)) and as functions of the k parameter with μ fixed (subplots (i)-(p)). One hundred trials, each of 1000 i.i.d. samples, were used for each data point.

Simulations were performed using a single-element focused (f/4) transducer with a center frequency of 10 MHz. The ideal transducer had a geometrical focal length of 50.8 mm and was excited with a Gaussian windowed sinusoidal pulse with a 50% fractional bandwidth at -6 dB. The -12 dB pulse-echo beamwidth of the transducer, approximated as $1.4\lambda f^{\#}$, where λ is the acoustic wavelength and $f^{\#}$ is the focal number of the transducer, was 0.86 mm. Simulations were performed using phantoms containing point scatterers. The echo signals received from the phantoms were sampled at 200 MHz. No noise was added in the simulations. A constant speed of sound of 1540 m/s was assumed.

The resolution cell volume was estimated by scanning a single point scatterer located at the focus of the transducer. Following Dutt and Greenleaf [14], the resolution cell was defined by the -20 dB contour of the envelope. Due to the circular symmetry of the beam pattern, the three-dimensional resolution cell was determined by the volume of revolution of the two-dimensional resolution cell about the axis of the transducer. This characterization procedure is illustrated in Figure 3.3. The resolution cell volume was found to be 0.184 mm^3.

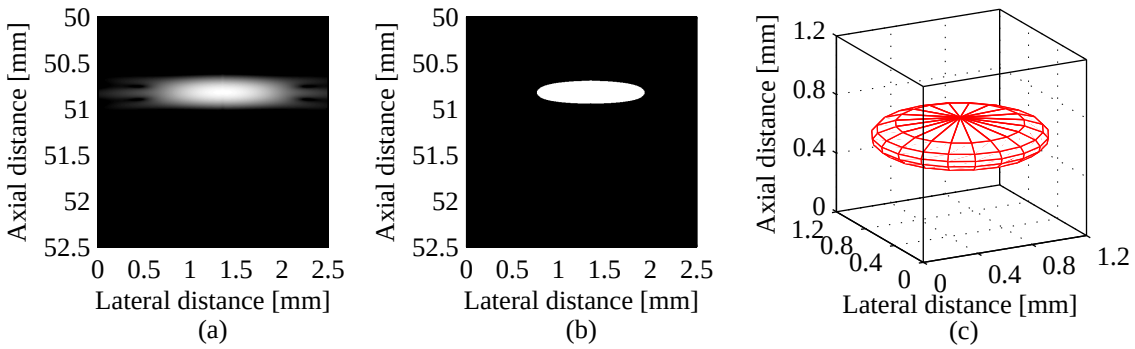

Figure 3.3. Characterization plots for the simulated 10 MHz transducer: (a) B-mode image of the scan of the single scatterer, (b) a two-dimensional representation of the -20 dB resolution cell, and (c) a three-dimensional depiction of the resolution cell.

3.2.1 Scatterer number density

Computational phantoms were constructed with scatterer number densities ranging from 1.0 to 10 scatterers per resolution cell in increments of one. For each of the 10 scatterer number densities examined, 10 independent phantoms were constructed by randomly placing point scatterers within a volume of height 17.2 mm, length 20.7 mm, and width 1.72 mm. The height was chosen to correspond to the approximate -6 dB depth of focus of the transducer, the length was chosen to be 24 beamwidths, and the width was chosen to be two beamwidths. The center of the volume was placed at the geometric focus of the transducer. A summary of the simulation setup is depicted in Figure 3.4.

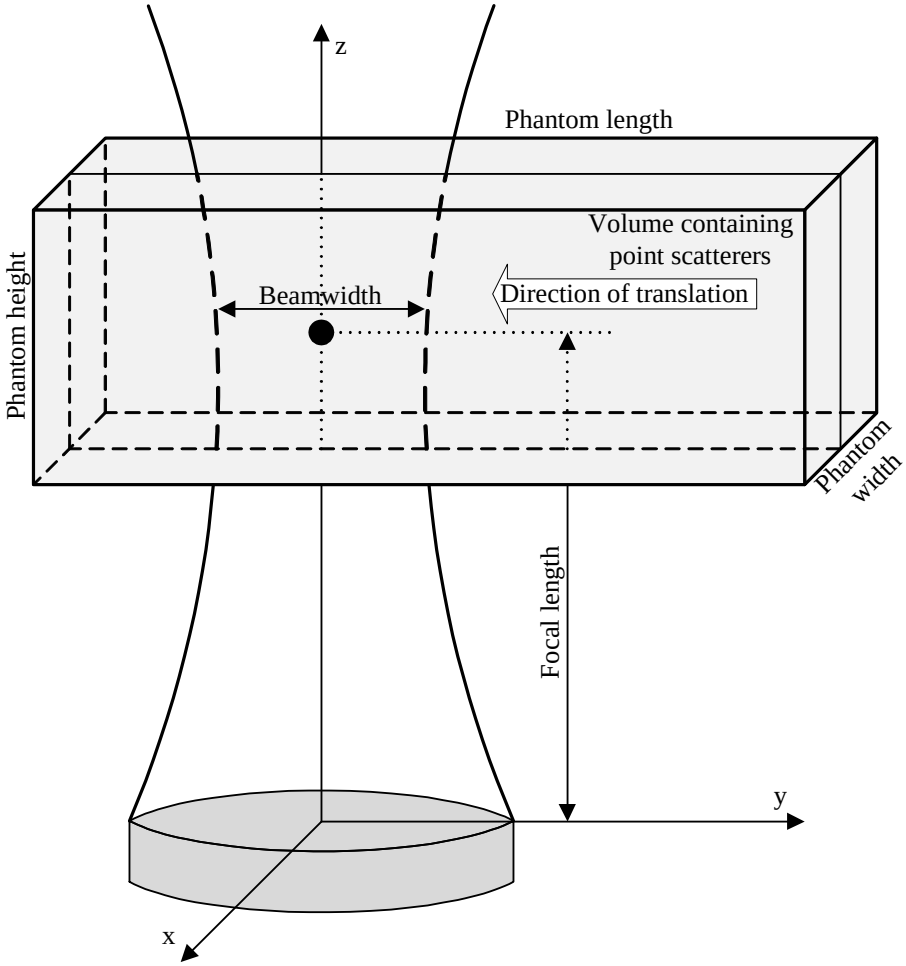

Figure 3.4. Illustration of the transducer (located at the origin) and the volume containing point scatterers used for simulations.

Radio frequency (RF) echo data was simulated for scan lines spaced 0.43 mm (i.e., half a beamwidth) apart. The envelope of the RF data for each scan line was detected using the Hilbert transform.

The envelopes for all the scan lines were aligned to form an image. The analysis of the image was divided into regions of interest (ROIs) sized approximately 2 mm $\times$ 2 mm and overlapped by 75% both laterally and axially. Envelope statistics model parameters were estimated for each ROI using the SNR, skewness, and kurtosis method described in Section 2.2. For each simulated image, the estimates from all ROIs were averaged together to produce a single pair (k, μ) of parameter estimates. The mean and SD of these average values were calculated from the 10 independent phantoms for each of the 10 scatterer number densities examined. The results are plotted in Figure 3.5.

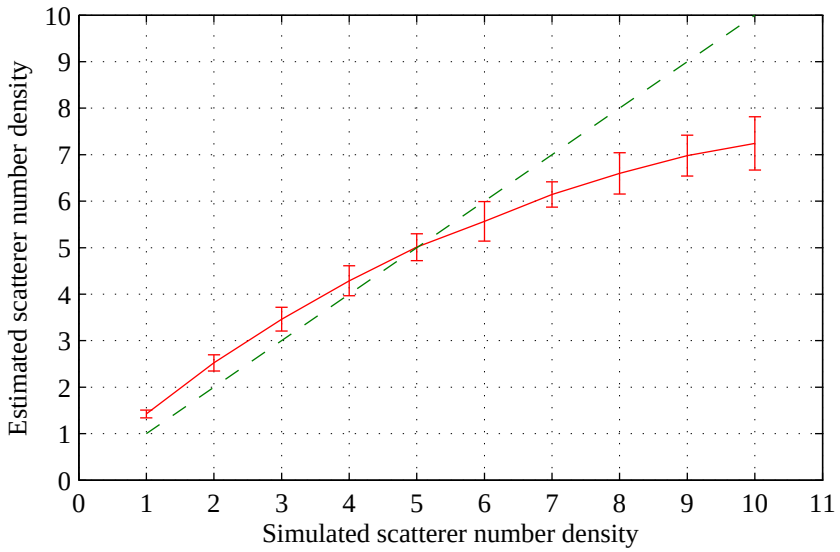

Figure 3.5. Estimated scatterer number density versus the actual scatterer number density for simulated phantoms. The error bars are two standard deviations long. Ideally the estimates would lie on the dashed green line.

The mean estimated scatterer number density increases monotonically as the actual scatterer number density increases, although the estimates show a positive bias for scatterer number densities less than five and a negative bias for scatterer number densities

greater than five. Also, there is a general increase in estimate variation with increased scatterer number density, as expected.

3.2.2 Scatterer clustering

Previous work [14], [44] has suggested that the presence of collections of closely grouped (i.e., clustered) scatterers alters the effective number of scatterers per resolution cell. One would expect a decrease in the μ parameter estimate with increased scatterer clustering. Computational phantoms were used to verify this hypothesis. The procedure used was the same as in the previous section, except that the average scatterer number density was kept at a constant value of eight scatterers per resolution cell and the scatterers were placed in the phantoms both randomly and in clusters. Figure 3.6 illustrates the random and clustered placement of scatterers. The number of clustered and the number of randomly placed scatterers were varied, with the total number of scatterers remaining constant to achieve the constant eight scatterers per resolution cell on average. In constructing each phantom, the clusters of scatterers were first placed randomly in the phantom and then the remaining scatterers were randomly placed. The number of scatterers in each cluster was random, being uniformly distributed on the interval from one through 20.

The analysis was performed in the same way as in the previous section. The results are shown in Figure 3.7. Note that the fraction of clustered scatterers is only an approximation because the randomly placed scatterers could cluster together by chance as well. The estimated scatterer number density in Figure 3.7 follows a monotonic decrease with increased scatterer clustering, as expected. Furthermore, for the case where all the scatterers were grouped into clusters, the actual scatterer number density of eight is

roughly 10 times the estimated scatterer number density of approximately 0.8. Based on the uniform distribution of the number of scatterers per cluster, an average value of 10.5 scatterers per cluster is expected. This indicates that each cluster was acting as a single scatterer in terms of envelope statistics in the simulations.

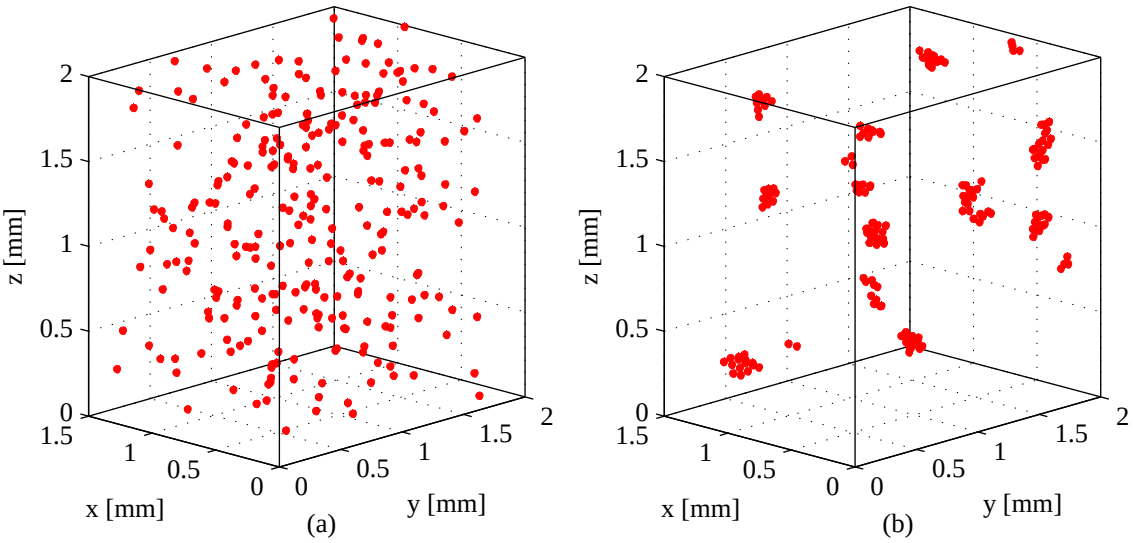

Figure 3.6. Depiction of the organizational structure of scatterers for the cases where (a) all scatterers were randomly located and (b) all scatterers were clustered. The remainder of the simulations lie between these two extremes with some fraction of the total number of scatterers clustered together and the rest of the scatterers randomly distributed throughout the phantom.

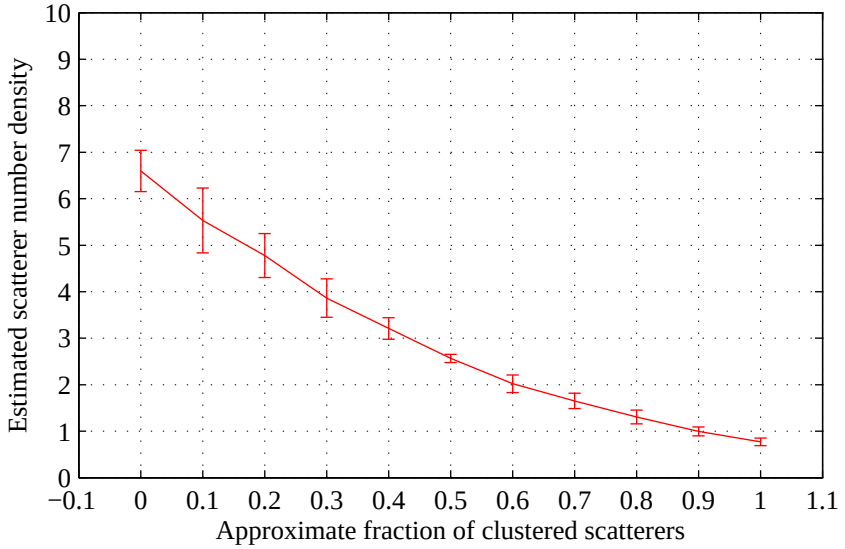

Figure 3.7. Estimated scatterer number density versus the approximate fraction of clustered scatterers for simulated phantoms. The error bars are two standard deviations long.

3.2.3 Scatterer periodicity

To test the ability of the homodyned K distribution to model echo signals with a large coherent component, computational phantoms with periodically located scatterers were created. The procedure used was the same as in the previous section where two scatterer populations were used, except that periodically located scatterers were used instead of clustered scatterers. The periodically located scatterers were created by first dividing the extent of the phantom along the z-axis into 100 bands of height 73.5 µm that were spaced 99.0 µm apart. Then, the scatterers were randomly placed inside the bands. Figure 3.8 illustrates an example of how the scatterers were placed periodically in bands.

The analysis was performed in the same way as in the previous two sections. The results are shown in Figure 3.9. Note that the fraction of periodically located scatterers is only an approximation because the randomly located scatterers may end up being periodically located by chance. The estimated *k* parameter in Figure 3.9 generally increases as the fraction of periodically located scatterers increases.

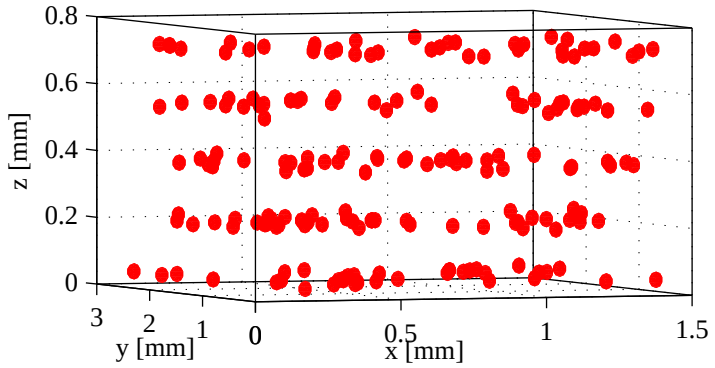

Figure 3.8. Depiction of the organizational structure of periodically located scatterers in a small portion of the simulated phantom. Here the scatterers occupy five horizontal bands.

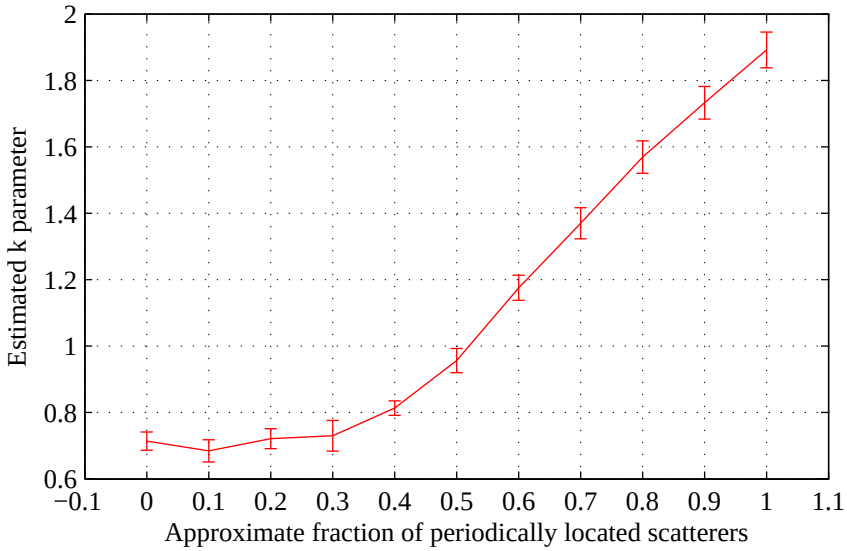

Figure 3.9. Estimated *k* parameter versus the approximate fraction of periodically located scatterers for simulated phantoms. The error bars are two standard deviations long.

3.3 Experimental Phantoms

3.3.1 Physical phantom

A phantom was prepared by suspending glass beads with diameters in the range of 150 µm to 180 µm in an agar background with a concentration of 3.96 beads per cubic millimeter. The glass beads were assumed to be uniformly distributed throughout the phantom and randomly separated. The phantom was scanned using five transducers with nominal center frequencies ranging from 2.25 MHz to 10 MHz. Five different images were acquired from different locations in the phantom using each transducer. The effective scatterer number density was estimated using small ROIs in each of the 25 resulting images. The estimates from all the ROIs in each image were averaged together to produce a single estimated scatterer number density for each image. The statistics (mean and SD) of these estimates for each set of five images are reported in Table 3.1. Table 3.1 also lists an estimate of the predicted scatterer number density which was determined based on the estimated resolution cell size and the bead concentration.

Table 3.1. Predicted and estimated (mean±SD) scatterer number densities for the physical phantom.

Transducer center frequency (MHz)	Estimated resolution cell volume (mm^3)	Predicted μ parameter	Estimated μ parameter	Deduced scatterer concentration (scatterers per mm^3)
2.25	3.52	13.9	7.46±1.4	2.12±0.40
3.5	1.26	4.99	5.67±0.45	4.50±0.36
5	0.505	2.00	1.61±0.15	3.19±0.30
7.5	0.227	0.900	1.00±0.22	4.40±0.97
10	0.0907	0.359	0.385±0.040	4.24±0.44

The resolution cell volume of each transducer was estimated in a way similar to that described in Section 3.2, except that a wire target technique [45] was used instead of a point scatterer to characterize each transducer. To carry out this technique, a thin wire was placed in the focal plane of each transducer and scanned. The resolution cell volume estimation was performed in the same way as described in Section 3.2. Plots illustrating the characterization procedure are shown in Figure 3.10.

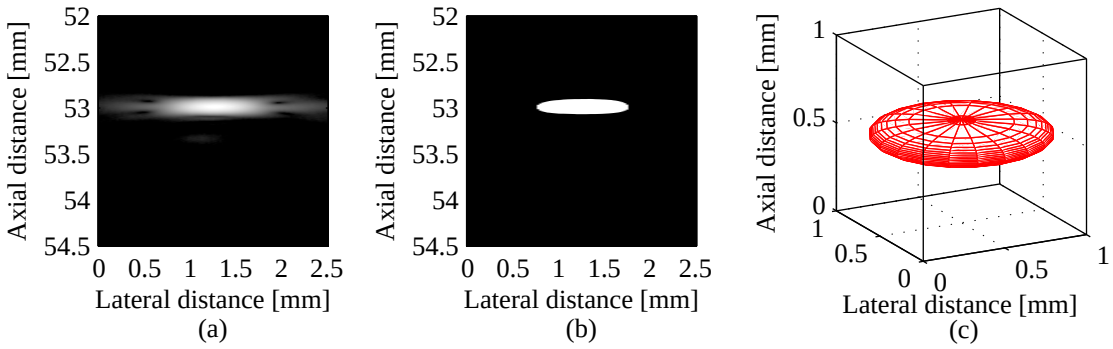

Figure 3.10. Characterization plots for the 10 MHz transducer used in the experiment: (a) B-mode image of wire target scan, (b) a two-dimensional representation of the -20 dB resolution cell, and (c) a three-dimensional depiction of the resolution cell.

For the cases where the number of scatterers is within the Rayleigh limit of 10 scatterers per resolution cell, the estimates agree relatively well with the theoretical predictions. For the case where the scatterer number density exceeds the Rayleigh limit, the estimates do not agree very well with the predictions. The trend in the estimates is correct nonetheless: the estimated scatterer number density increases with increased resolution cell volume.

3.3.2 Biological phantoms

Four biological phantoms were prepared by suspending 4T1 mouse mammary tumor cells in a 2% agar base. Each phantom was prepared with a different concentration of 4T1 cells as shown in Table 3.2. The phantoms were assumed to contain cells uniformly spread throughout the phantom with random spatial locations. Each phantom was scanned using three different focused (f/3) single-element transducers with nominal center frequencies of 10 MHz, 20 MHz, and 40 MHz. The 12 resulting B-mode images are shown in Figure 3.11.

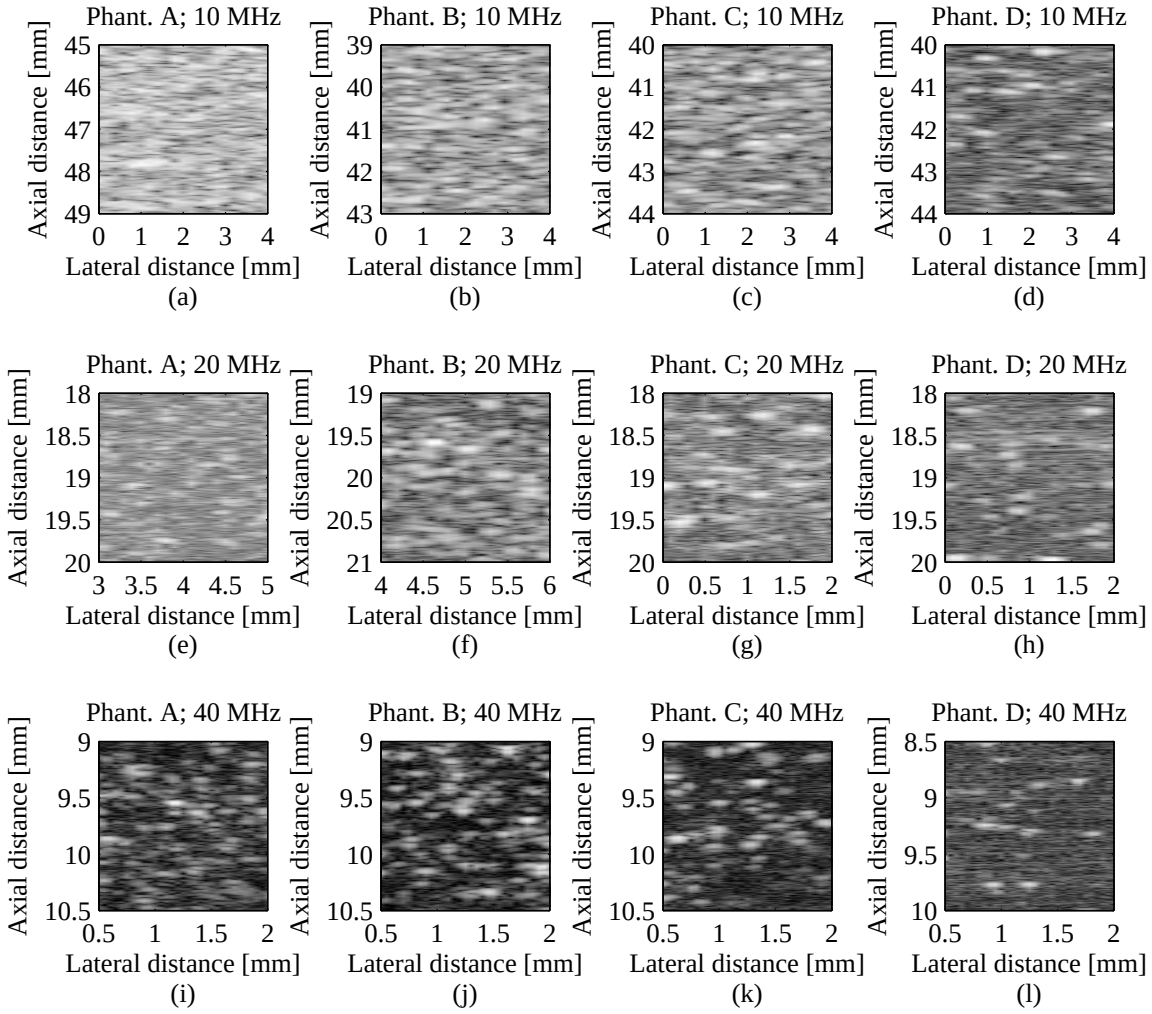

Figure 3.11. B-mode images of biological phantom scans.

Table 3.2. Cell concentrations used in biological phantoms.

Phantom	Cell concentration (cells/mm^3)
A	1000
B	500
C	100
D	50

Each image was divided into many small ROIs for analysis. Parameters from the envelope statistics model were estimated for each ROI. The mean and SD of the estimated scatterer number densities for all the ROIs in each phantom are reported in Table 3.3. The expected scatterer density was also deduced from the nominal cell concentrations in Table 3.2 and the resolution cell volume which was determined using the same wire target technique as described in the previous section. The theoretical predictions based on the estimated resolution cell size and the known number density of cells in the phantoms are listed in Table 3.4.

The estimates follow the expected trends: lower cell concentrations resulted in lower estimates of scatterer number density, and higher frequencies also resulted in lower estimates. However, comparison of Tables 3.3 and 3.4 shows that the estimated scatterer number densities were observed to be substantially lower than the theoretical predictions. Closer examination of the B-mode images in Figure 3.11 reveals that in many cases individual scatterers can be resolved. For example, individual scatterers can be resolved in Figure 3.11(d); however, the theoretical scatterer number density is 2.63 scatterers per resolution cell. The estimate of 0.356 scatterers per resolution cell is more consistent with the B-mode images. These large discrepancies may be attributed to the clustering of cells, which would violate the assumption that the cells were uniformly distributed throughout the phantom.

Table 3.3. Estimated scatterer number densities (mean±SD) for biological phantoms.

Phantom	10 MHz	20 MHz	40 MHz
A	7.30±5.4	1.34±0.96	0.264±0.19
B	1.26±0.72	0.596±0.47	0.145±0.071
C	0.773±0.41	0.308±0.12	0.120±0.049
D	0.356±0.44	0.264±0.11	0.0981±0.063

Table 3.4. Theoretical scatterer number densities for biological phantoms.

Phantom	10 MHz	20 MHz	40 MHz
A	52.5	11.2	3.22
B	26.3	5.61	1.61
C	5.25	1.12	0.322
D	2.63	0.561	0.161

To examine the clustering of cells, the phantoms were formalin-fixed, paraffin-embedded, and sliced into sections approximately 3 µm thick. Each section was mounted on a glass slide and stained with Hematoxylin and Eosin. The slides were examined under a light microscope and photomicrographs were captured with a camera. Figure 3.12 shows photomicrographs of the four phantoms. In general, the biological phantoms with higher cell concentrations had more and larger clusters of cells, thus helping to explain the discrepancies between the theoretical and estimated scatterer number densities.

3.4 Animal Data

3.4.1 Sarcomas and carcinomas

Rodent models of breast cancer were used to test the ability of envelope-based statistics in distinguishing two kinds of tumors. Ten mouse mammary carcinoma tumors and 10 mouse mammary sarcoma tumors were scanned at 20 MHz. Each tumor image was analyzed by estimating envelope statistics model parameters for ROIs sized approximately 1 mm $\times$ 1 mm in the tumor image. The model parameters from all the ROIs in each tumor were averaged together to produce a single pair of parameter estimates for each tumor.

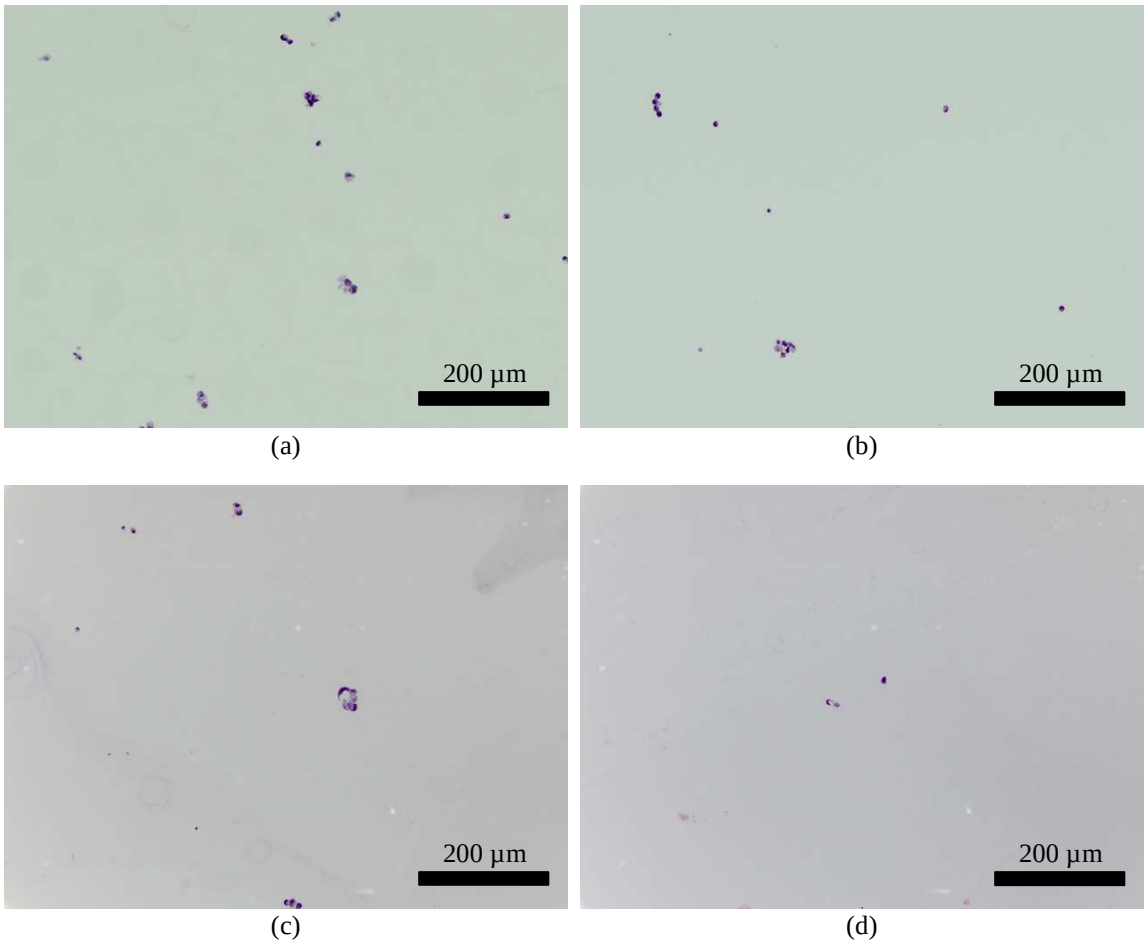

(a) (b)

(c) (d)

Figure 3.12. Photomicrographs of biological phantoms: (a) phantom A, (b) phantom B, (c) phantom C, and (d) phantom D.

These parameters are plotted in Figure 3.13. The line separating the two classes of tumors was derived using a support vector machine. This line was used to derive a third parameter to combine the two model parameters and further discriminate between the two kinds of tumors. Letting the equation of the line separating the two kinds of tumors be defined as $k = m\mu + b$, the derived parameter D was defined as

$$D = \hat{k} - m\hat{\mu} \tag{3.7}$$

where $\hat{k}$ and $\hat{\mu}$ are the two average estimated model parameters for each tumor.

Table 3.5 lists the statistics of the estimated model parameters for the 20 tumors. Of the two estimated parameters, only the k parameter is statistically significant in

distinguishing between the two kinds of tumors. However, the parameter derived from a linear combination of the two estimated model parameters is more statistically significant than either parameter alone.

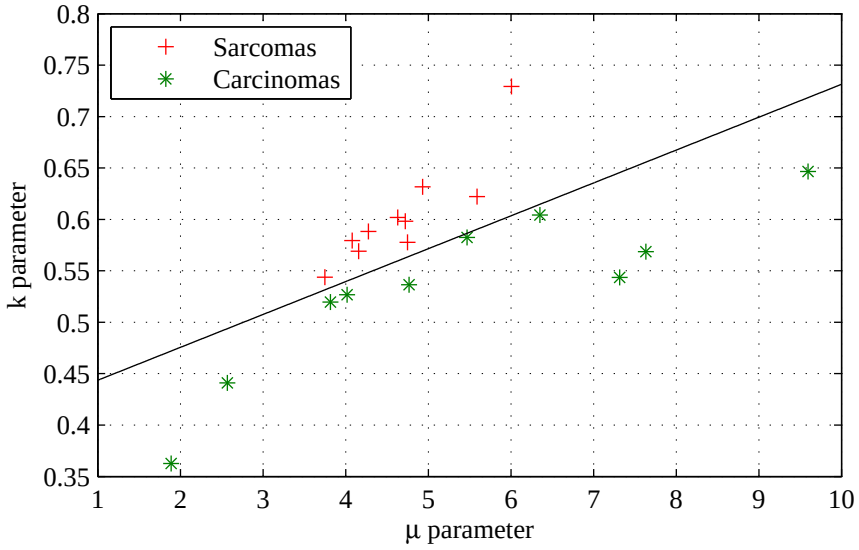

Figure 3.13. Scatter plot of the average estimated model parameters for sarcoma and carcinoma tumors.

Table 3.5. Estimated model parameters (mean±SD) for sarcoma and carcinoma tumors.

Kind of tumor	k	μ	D
Sarcomas	0.604±0.051	4.69±0.69	0.454±0.033
Carcinomas	0.533±0.081	5.34±2.4	0.362±0.041
	$p<0.05$	$p=0.421$	$p<0.0001$

3.4.2 Sarcomas, carcinomas, and fibroadenomas

Fourteen mouse mammary carcinoma tumors, six mouse mammary sarcoma tumors, and 11 rat fibroadenoma tumors were scanned at 10 MHz. Parameter estimation and processing were performed in the same way as in the previous section, except that larger ROIs (roughly 2 mm $\times$ 2 mm) were used because of the lower transducer frequency used. The average estimated model parameters are plotted in Figure 3.14; the mean and SD of the parameter estimates for each kind of tumor are listed in Table 3.6. One-way analysis of variance (ANOVA) was performed pairwise between the different kinds of

tumors for each of the two estimated model parameters. The resulting p-values are listed in Table 3.7. Again, statistically significant differences were observed only in the *k* parameter estimates.

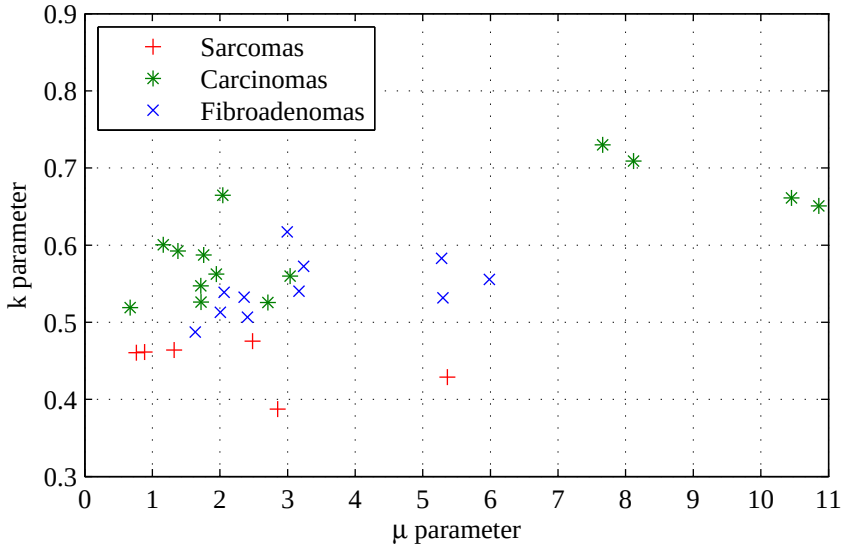

Figure 3.14. Scatter plot of the average estimated model parameters for sarcoma, carcinoma, and fibroadenoma tumors.

Table 3.6. Estimated model parameters (mean±SD) for sarcoma, carcinoma, and fibroadenoma tumors.

Kind of tumor	*k*	μ
Sarcomas	0.446±0.033	2.28±1.7
Carcinomas	0.603±0.070	3.95±3.6
Fibroadenomas	0.543±0.037	3.31±1.5

Table 3.7. P-values for model parameter estimates comparing different kinds of tumors.

Kinds of tumors compared	*k*	μ
Sarcomas & carcinomas	p<0.0001	p=0.302
Sarcomas & fibroadenomas	p<0.0001	p=0.220
Carcinomas & fibroadenomas	p<0.05	p=0.593

CHAPTER 4
FACTORS AFFECTING ESTIMATES

4.1 Introduction

Parameter estimates obtained from the homodyned K distribution model are useful for characterizing the medium being interrogated. However, the performance of parameter estimates is affected by a number of factors besides those of the medium. The usefulness of these parameter estimates can only be optimized when these other factors are well understood.

4.2 Region of Interest Size

Quantitative ultrasound (QUS) images are created by dividing the corresponding B-mode image into a number of ROIs to image differences in the underlying material properties. Furthermore, statistical analysis can be used to quantify the variability of estimates throughout the image. In general, estimate bias and variation will be smaller for large ROIs and larger for small ROIs. Therefore, there is a fundamental tradeoff to be made between the spatial resolution and the bias and variation of parameter estimates. This tradeoff was studied using ideal random samples, simulations, and phantom data.

4.2.1 Independent random samples

All else being equal, when a larger ROI is used, a greater number of envelope samples are available for estimation. As a first step towards examining the effects of sample size on estimate bias and variation, i.i.d. samples of the homodyned K distribution

were generated using the method outlined in Section 3.1.1. Because the samples are statistically independent and follow the desired distribution exactly, this analysis should establish a best-case theoretical limit.

Sets of samples were generated for a variety of model parameters: μ ranging from 1.0 to 10 and k ranging from 0.25 to 1.0. For each sample size and pair of parameter values, 50 independent estimation trials were performed. The absolute relative bias and the normalized SD of the parameter estimates were calculated. For each sample size, the average absolute relative bias was computed by averaging together the absolute relative bias obtained from the 50 trials for each set of parameter values. The average normalized SD was obtained similarly. The absolute relative bias (given by the absolute value of Equation (3.5)) was used instead of the relative bias to allow meaningful averaging of the biases from different trials. The results, plotted in Figure 4.1, follow expectations.

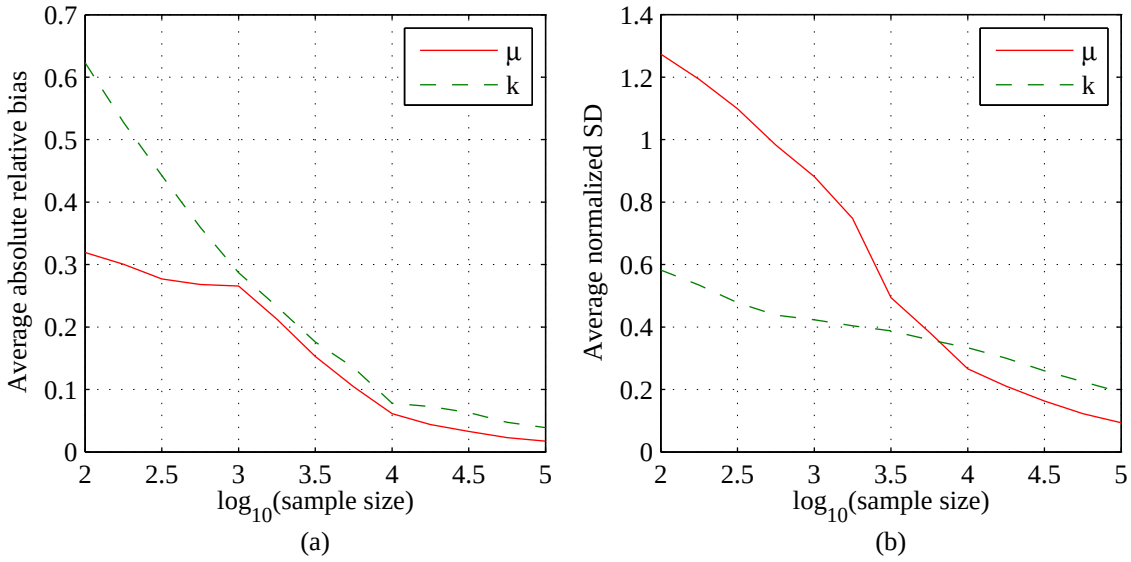

Figure 4.1. Average absolute relative bias and average normalized SD of estimated model parameters versus sample size.

4.2.2 Simulations

Ten images with underlying scatterer number densities ranging from 1.0 to 10 scatterers per resolution cell from the simulations performed for Section 3.2.1 were re-analyzed using ROIs of varying lateral and axial size. For each image and for each ROI size, the absolute relative bias and the normalized SD of the k and μ parameters were calculated. To calculate these performance metrics, the true parameter values must be known. For the μ parameter, the intended scatterer number density was used as the true value of μ; for the k parameter, a very large ROI was used to obtain the best possible estimate of the true value of k. For each ROI size examined, the average absolute relative bias and average normalized SD were determined by averaging together the results from the 10 independent phantoms. Because both the pulse length and beamwidth are proportional to the acoustic wavelength, the results are reported with the dimensions in wavelengths. The results should therefore be generalizable to data acquired using different transducer frequencies.

The average normalized SD for the two model parameters is shown in Figure 4.2 and the average absolute relative bias for the two model parameters is shown in Figure 4.3. The decrease in the normalized SD of the μ and k parameter estimates as the ROI size is increased is fairly smooth, agreeing with expectations. The absolute relative bias for the μ parameter is largest for the smallest ROI size used, but it does not show any particularly meaningful decrease for ROIs larger than about 10 wavelengths, suggesting that an ROI size of 10 wavelengths is optimal for reducing estimate bias while maintaining spatial resolution.

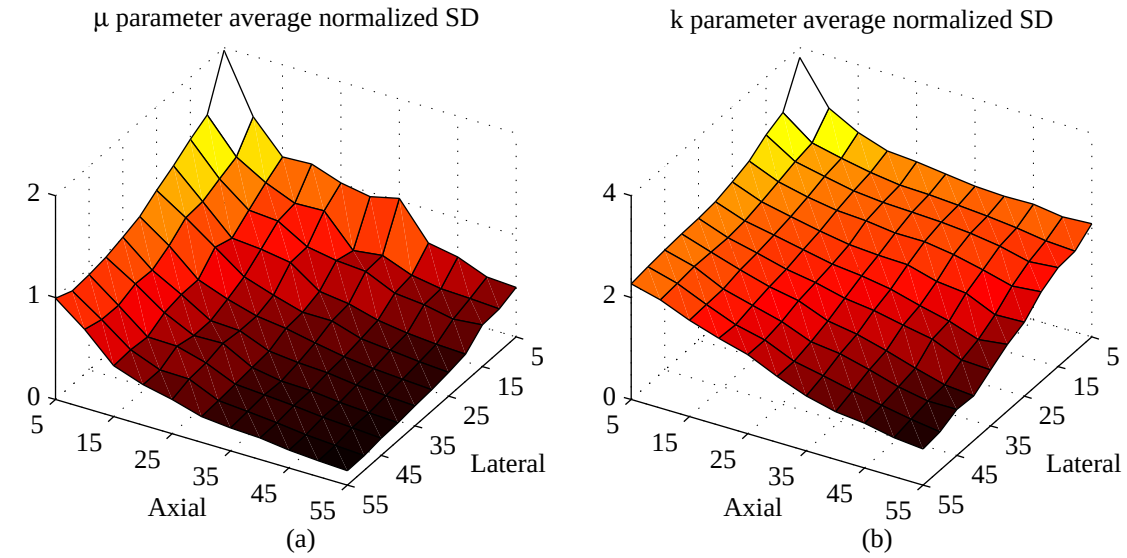

Figure 4.2. Average normalized SD of estimated model parameters for simulated phantom scans versus the axial and lateral extent (in wavelengths) of the ROIs used.

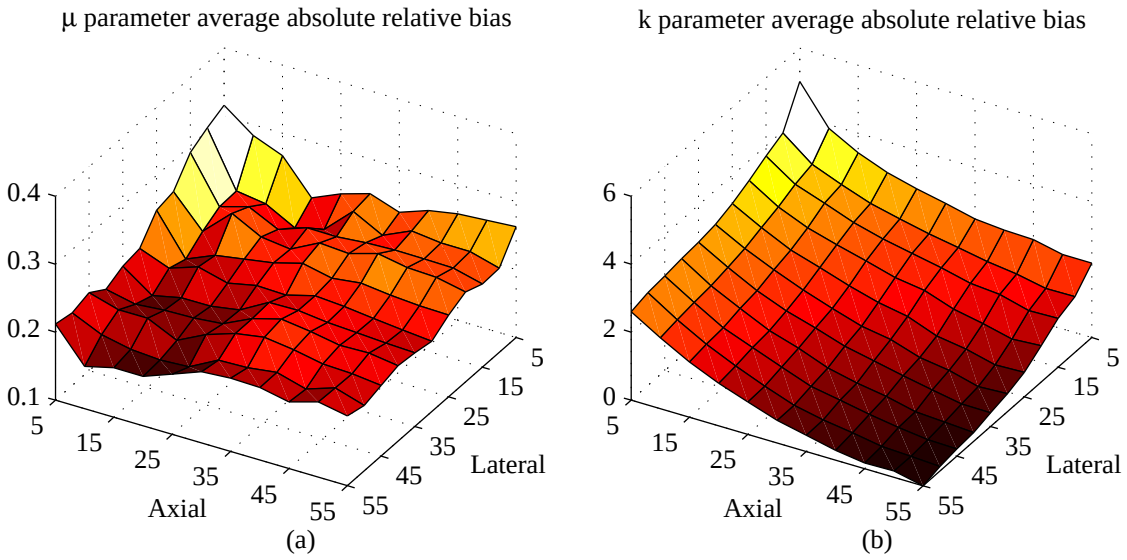

Figure 4.3. Average absolute relative bias of estimated model parameters for simulated phantom scans versus the axial and lateral extent (in wavelengths) of the ROIs used.

4.2.3 Phantoms

Two phantoms containing different concentrations of glass bead scatterers were constructed. Each phantom was scanned using an f/4 transducer with center frequency of 10 MHz. As in Section 4.2.2, model parameters based on envelope statistics were

estimated using a range of ROI sizes. The absolute relative bias and normalized SD were calculated using the parameter estimates from the largest ROI as the true parameter values. To produce a smoother, more representative plot, the absolute relative bias and the normalized SD for each ROI size from the two phantoms were averaged together; the results are shown in Figures 4.4 and 4.5. In general, the results obtained by analyzing the physical phantoms agree with the results from the simulations and with expectations.

Finally, it should be noted that while very large ROIs generally worked well for these studies (where the material properties are fairly homogenous), the use of large ROIs in practice can be problematic if the underlying properties of the medium vary substantially throughout the ROI. Therefore, the goal is to minimize the size of the ROI for optimal spatial resolution versus bias and variation in estimates and to increase the likelihood of uniform scattering statistics in each ROI.

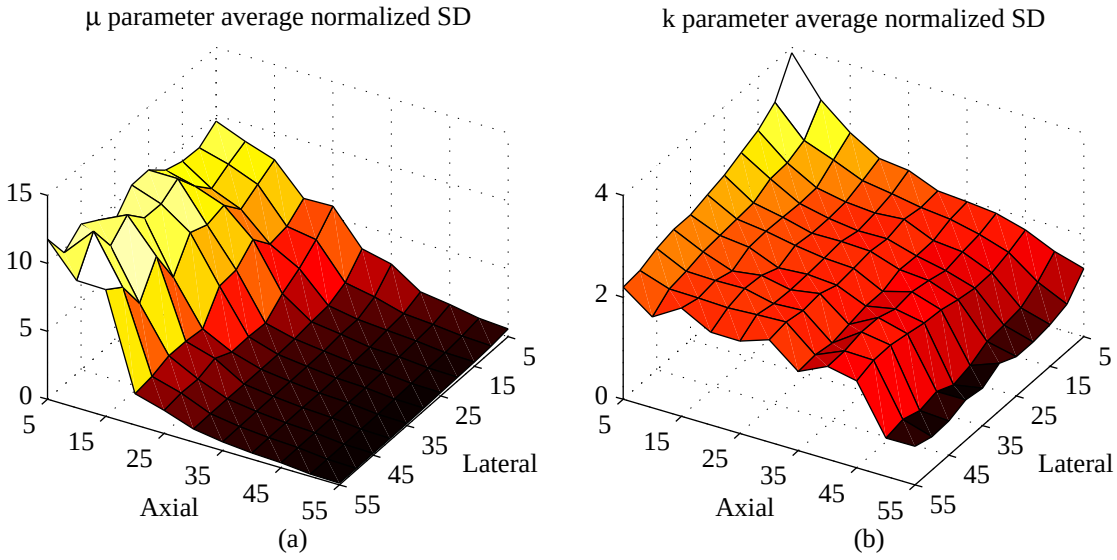

Figure 4.4. Average normalized SD of estimated model parameters for experimental phantom scans versus the axial and lateral extent (in wavelengths) of the ROIs used.

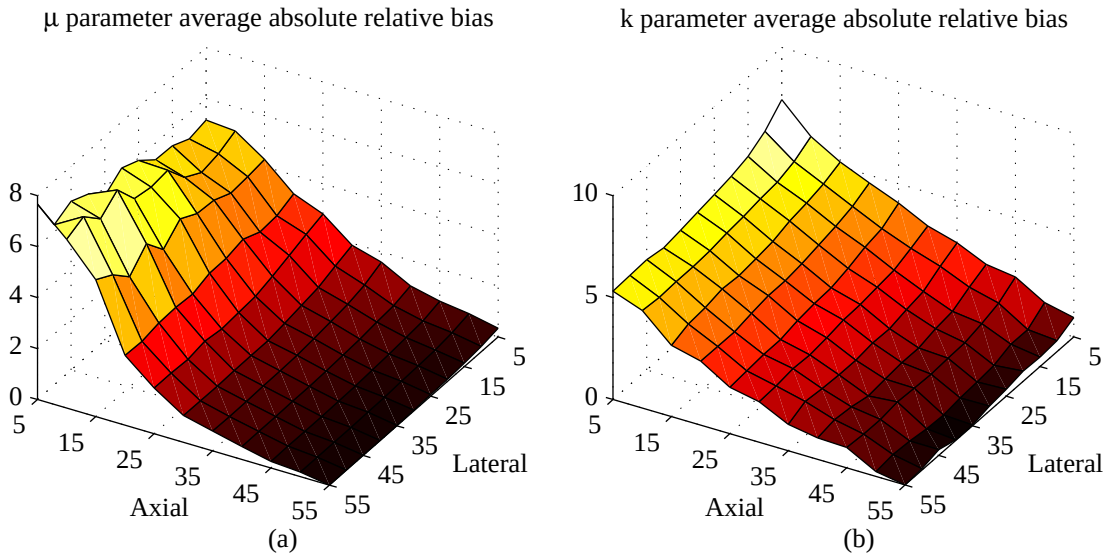

Figure 4.5. Average absolute relative bias of estimated model parameters for experimental phantom scans versus the axial and lateral extent (in wavelengths) of the ROIs used.

4.3 Resolution Cell Size

The μ parameter of the homodyned K distribution quantifies the effective number of scatterers per resolution cell. To correctly interpret this parameter, the resolution cell volume must be known. The dimensions of the resolution cell are determined not only by properties of the transducer but also by properties of the medium including frequency dependent attenuation.

4.3.1 Transducer frequency

The resolution cell can be modeled as a cylinder with radius $r \propto \lambda$ and height $h \propto \lambda / B$, where B is the fractional bandwidth of the imaging pulse. Therefore, the volume of the resolution cell is proportional to λ^3 / B, or equivalently, inversely proportional to $f^3 B$, where f is the transducer center frequency. Therefore, the estimated scatterer number density (scatterers per resolution cell) is expected to decrease with the third power of the frequency.

Computer simulations were performed to verify these predictions. Ten independent computational phantoms were created. Each phantom was scanned using eight different transducers with center frequencies ranging from 6 MHz to 20 MHz. All the simulated transducers were focused (f/4) with a focal length of 50.8 mm. The transducers were excited with Gaussian modulated sinusoidal pulses with 50% fractional bandwidth at -6 dB. To accommodate the expected beamwidths and depths of focus of all eight transducers, all the phantoms were sized $8.62\ \text{mm} \times 10.3\ \text{mm} \times 2.87\ \text{mm}$. An average scatterer number density of 10 scatterers per resolution cell (based on the resolution cell volume of the 6 MHz transducer) was used for all phantoms. The simulated B-mode images obtained from one of the 10 phantoms are shown in Figure 4.6.

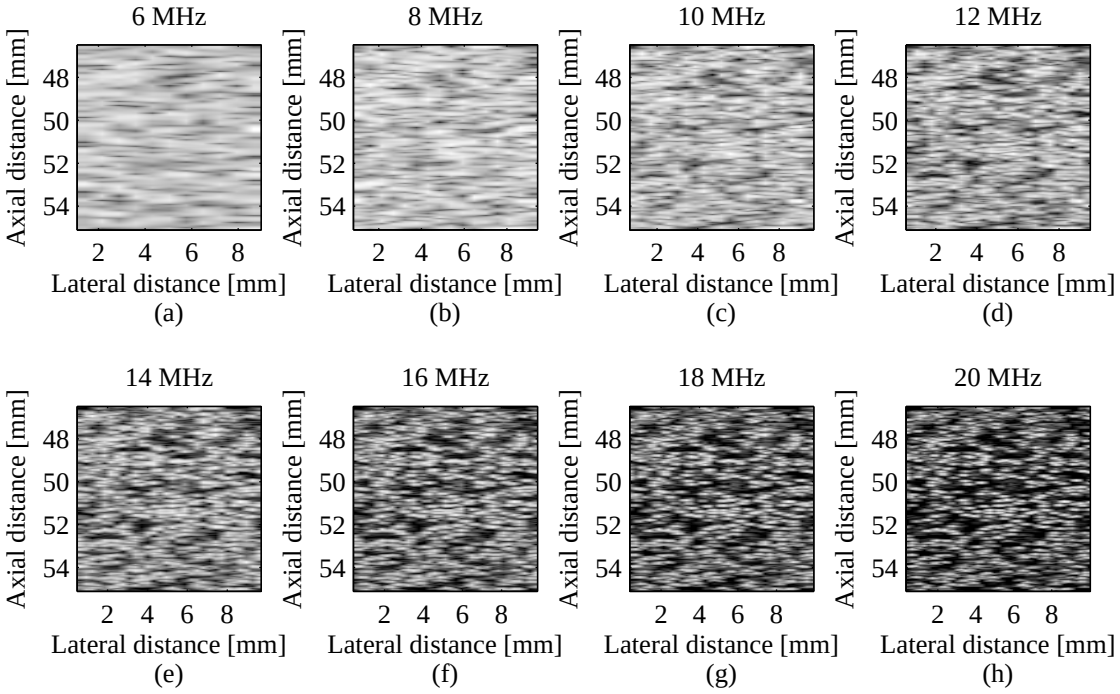

Figure 4.6. Simulated B-mode images using transducers with center frequencies ranging from 6 MHz to 20 MHz.

The scatterer number density for each image was estimated using techniques similar to those used in Section 3.2.1. For each transducer frequency used, the estimates

from the 10 independent phantoms were averaged together to produce the results shown in Figure 4.7. The scatterer number density predicted by the change in resolution cell volume is also plotted. The results of the simulations and the theory are generally in good agreement.

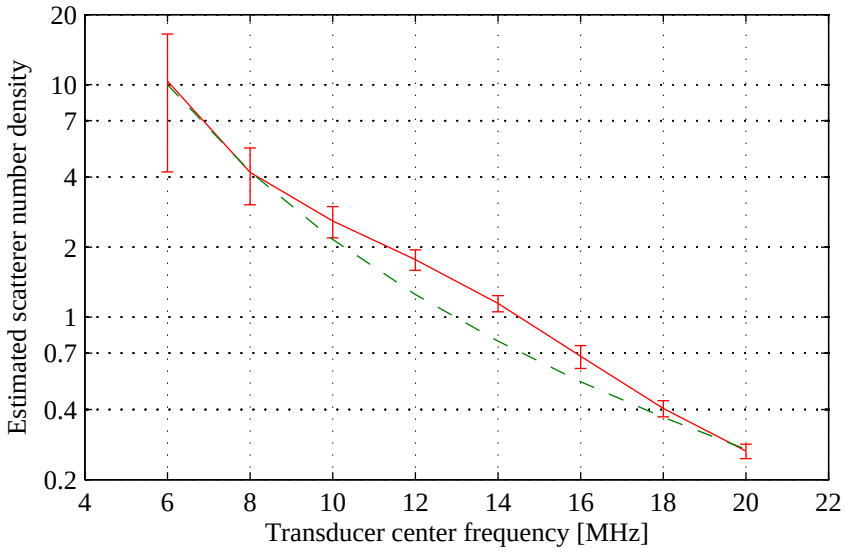

Figure 4.7. Estimated scatterer number density versus transducer frequency for simulated phantoms scanned at different frequencies. The error bars are two standard deviations long; note the use of log scaling on the vertical axis. Ideally, the estimates would lie on the dashed green curve.

4.3.2 Attenuation

4.3.2.1 Theory

Attenuation can be modeled as multiplication (in the frequency domain) of the Fourier transform of the imaging pulse by $e^{-x\alpha_0 f}$, where x is the pulse-echo distance from the transducer to the region being imaged, α_0 is the linear attenuation coefficient, and f is the frequency [12]. The frequency-dependent attenuation results in higher frequencies being attenuated more rapidly with depth than lower frequencies, producing a shift in the center frequency of the imaging pulse. Assuming a Gaussian pulse, the shift in center frequency, Δf, is given by [12]

$$\Delta f = f' - f_0 = \frac{-\alpha_0 x \left(2.66 f_0 B\right)^2}{4\pi^2} \tag{4.1}$$

where f' and f_0 are the center frequencies of the pulse with and without attenuation, respectively.

Approximating the resolution cell as a cylinder as in Section 4.3.1 and assuming that the fractional bandwidth is unchanged by attenuation, the ratio of the volume of the resolution cell in the presence of attenuation (V') to the volume of the resolution cell without attenuation (V) is given by

$$\frac{V'}{V} = \left(\frac{f_0}{f'}\right)^3 \tag{4.2}$$

Combining Equations (4.1) and (4.2) yields

$$\frac{V'}{V} = \left(\frac{4\pi^2}{4\pi^2 - (2.66)^2 \alpha_0 f_0 x B^2}\right)^3 \tag{4.3}$$

The estimated scatterer number density (scatterers per resolution cell) should increase according to the increase in the volume of the resolution cell predicted by Equation (4.3).

4.3.2.2 Simulations

Computational phantoms were used to verify the predictions in Section 4.3.2.1. Ten independent phantoms were generated for each attenuation coefficient value used. Each phantom was scanned using two imaging pulses with different fractional bandwidths. Each resulting image was analyzed using the approach described in Section 3.2.1. The results shown in Figure 4.8 were obtained by averaging the estimated scatterer number density from the 10 independent phantoms used for each attenuation coefficient. Both the theoretical and estimated scatterer number densities vary substantially as the attenuation coefficient changes when the phantoms were imaged using a pulse with 50%

fractional bandwidth (Figure 4.8(a)). By reducing the fractional bandwidth to 25%, this variation was reduced substantially (Figure 4.8(b)). These results are consistent with previously reported measurements of physical phantoms [46]. Note that the reduction in fractional bandwidth results in the use of a longer imaging pulse, reducing the axial resolution of the resulting image. Also, this increases the volume of the resolution cell in the absence of attenuation. When the scatterer number density is large, it is desirable to reduce the volume of the resolution cell to avoid exceeding the Rayleigh limit of about 10 scatterers per resolution cell beyond which scatterer number density estimation becomes unreliable.

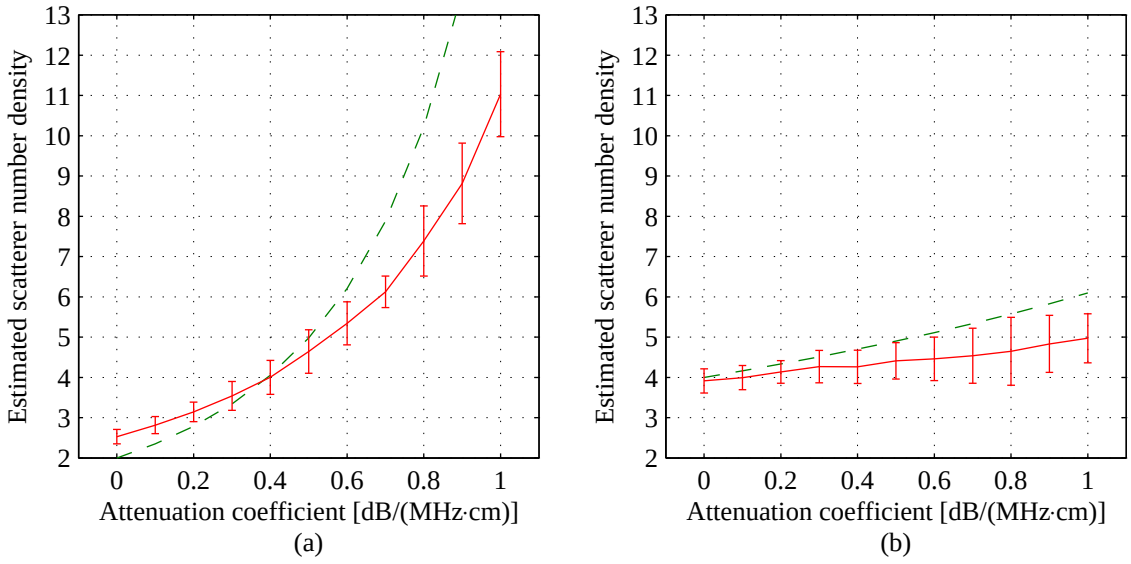

Figure 4.8. Estimated scatterer number density for simulated phantoms versus attenuation coefficient using a pulse with (a) 50% fractional bandwidth and (b) 25% fractional bandwidth. The error bars are two standard deviations long. Ideally, the estimates would lie on the dashed green curves which were determined using Equation (4.3).

4.4 Compounding

4.4.1 Spatial compounding

When analyzing an image using a number of small ROIs, the ROIs can be partially overlapped, or spatially compounded, to increase the number of ROIs available

for analysis. Furthermore, by spatially averaging the parameter estimates from each ROI based on the ROI overlap, the variation of estimates can be reduced at the cost of decreased spatial resolution.

4.4.1.1 Simulations

Following Section 4.2.2, 10 images with underlying scatterer number densities ranging from 1.0 to 10 scatterers per resolution cell were re-analyzed using ROIs overlapping by differing amounts to determine the impact on estimate bias and variation. The estimates were spatially averaged together based on the ROI overlap. The normalized SD and absolute relative bias were calculated from the spatially averaged estimates in the same way as in Section 4.2.2. The results are shown in Figures 4.9 and 4.10.

Analysis of the plots in Figure 4.9 suggests that spatial compounding reduces the SD of the estimates of the k parameter but has little effect on the SD of the μ parameter. The absolute relative bias of parameter estimates does not exhibit any significant decrease as ROI overlap is increased. A likely explanation for these results is that estimate bias is dictated by ROI size. Therefore, the bias is approximately the same for each ROI, and no amount of averaging will reduce it. Averaging will, however, reduce the variation about the mean estimated value.

Figure 4.9(b) suggests that the SD of the k parameter estimates can be made arbitrarily small by simply increasing the amount of ROI overlap. However, as the amount of ROI overlap is increased, the estimates become increasingly correlated because they share more of the same underlying samples of the envelope amplitude. At some point the improvement in estimate SD should level off.

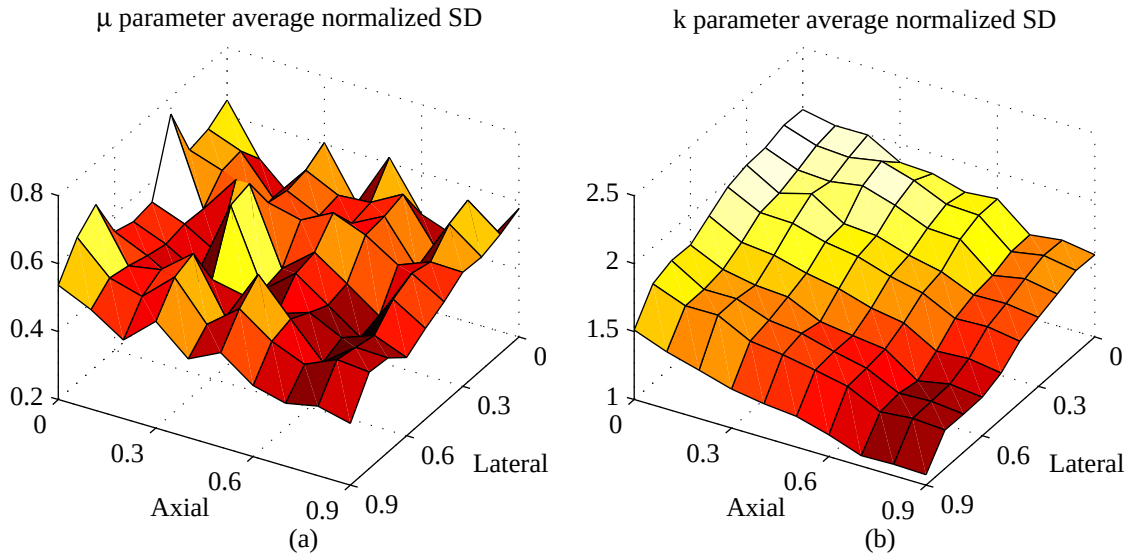

Figure 4.9. Average normalized SD of estimated model parameters for simulated phantom scans versus the fraction of axial and lateral overlap of the ROIs used.

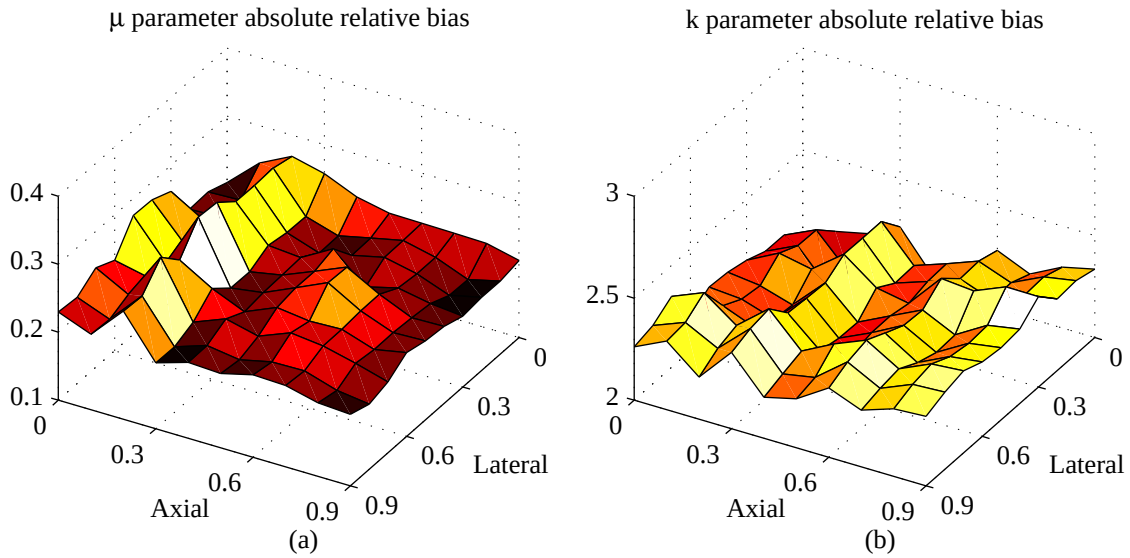

Figure 4.10. Average absolute relative bias of estimated model parameters for simulated phantom scans versus the fraction of axial and lateral overlap of the ROIs used.

The degree of correlation was quantified by calculating correlation coefficients for estimated model parameters for axially and laterally overlapping ROIs. Each correlation was run on two vectors corresponding to all pairs of ROIs overlapped (either axially or laterally) by a given amount. The correlation coefficients versus the fraction of

ROI overlap are plotted in Figure 4.11. It is reasonable to expect some degree of correlation between ROIs that do not overlap at all because the estimated model parameters should describe the same underlying material properties. These results agree with expectations: the amount of correlation in the parameter estimates increases as the fraction of ROI overlap is increased.

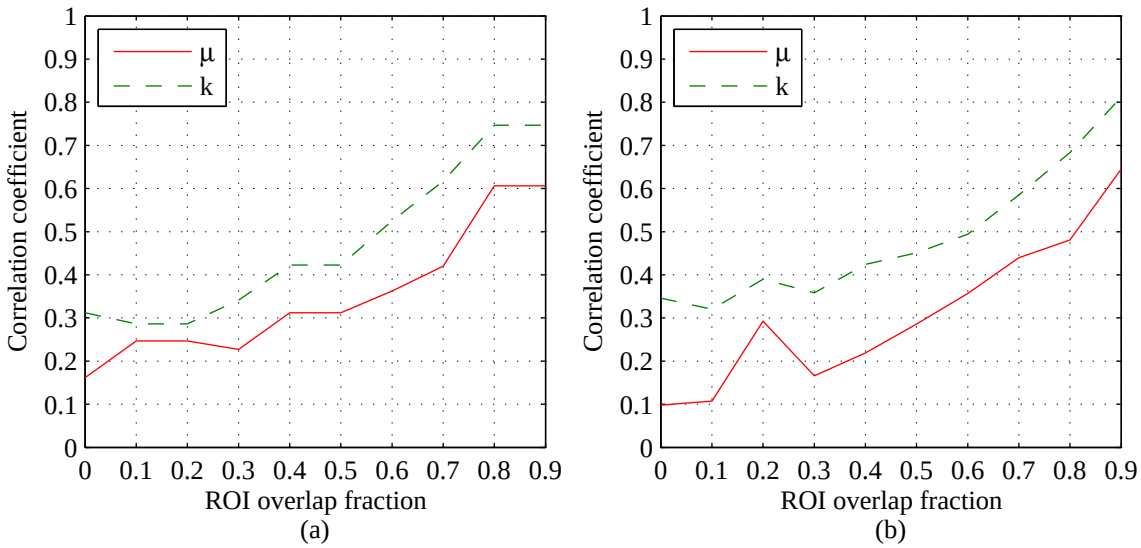

Figure 4.11. Correlation coefficients of estimated model parameters versus ROI overlap fraction for simulated phantom scans for (a) laterally overlapping ROIs and (b) axially overlapping ROIs.

4.4.1.2 Phantoms

The phantoms first described in Section 4.2.3 were also analyzed using varying amounts of spatial compounding using the same approach as in the previous section. The results (plotted in Figures 4.12 and 4.13) are generally consistent with the results obtained from the simulations. That is, only the SD in estimates of the *k* parameter shows any significant decrease with increased spatial compounding. The results from the physical phantoms are much noisier than the results from the simulations because of noise inherent in the experiment and because only two images were averaged together for the experimental phantom analysis, whereas 10 were used for the simulations.

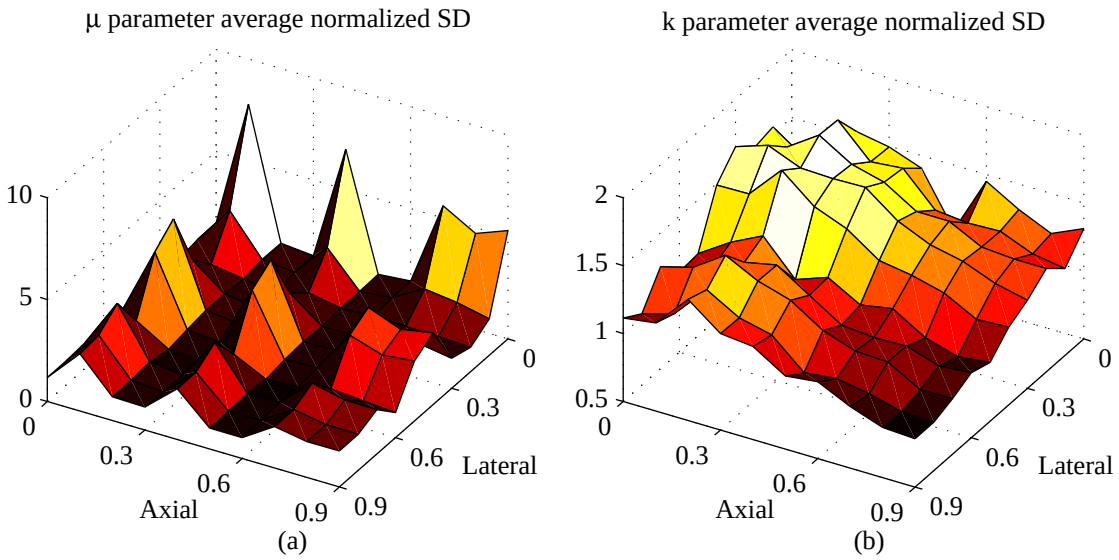

Figure 4.12. Average normalized SD of estimated model parameters for experimental phantom scans versus the fraction of axial and lateral overlap of the ROIs used.

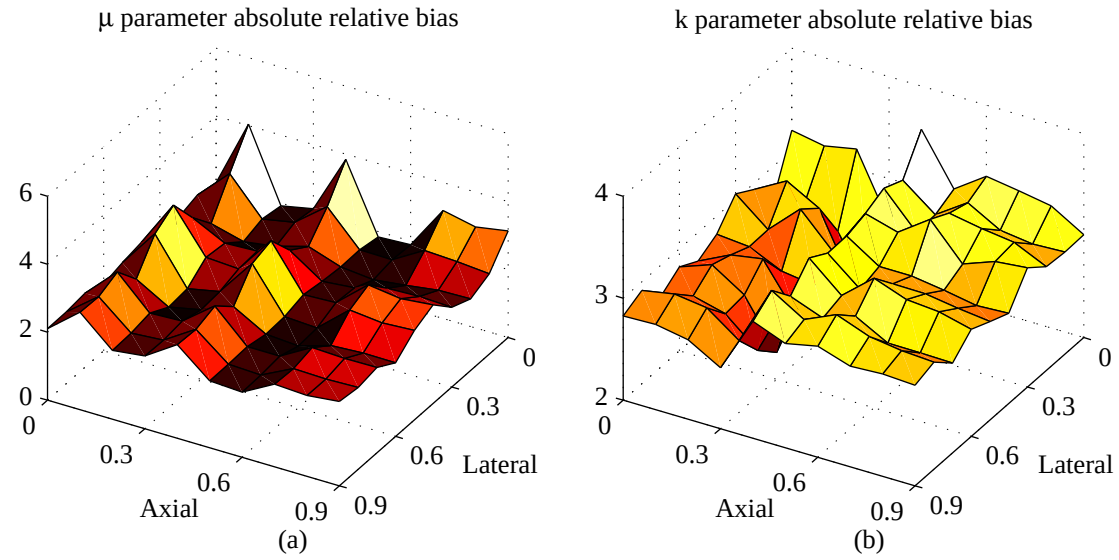

Figure 4.13. Absolute relative bias of estimated model parameters for experimental phantom scans versus the fraction of axial and lateral overlap of the ROIs used.

The correlation coefficients between parameter estimates for overlapping ROIs were also determined in the same way as in the previous section. The results are plotted in Figure 4.14. Observe that the correlation coefficient is negative in some cases.

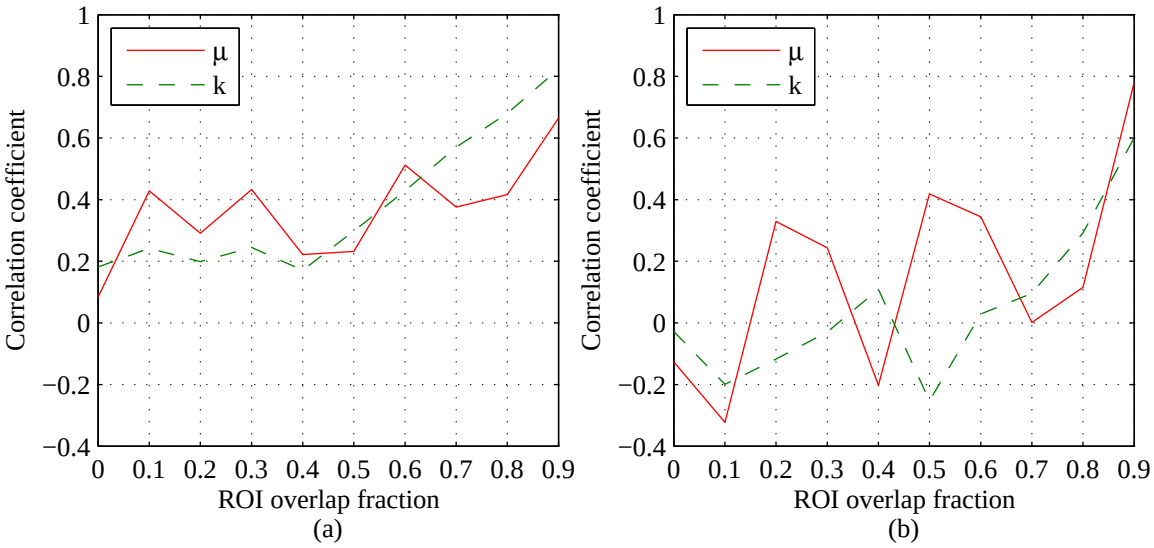

Figure 4.14. Correlation coefficients of estimated model parameters versus ROI overlap fraction for experimental phantom scans for (a) laterally overlapping ROIs and (b) axially overlapping ROIs.

4.4.2 Angular compounding

4.4.2.1 Introduction

Angular compounding, the acquisition and averaging of a number of different (partially correlated to uncorrelated) images of the same target, has been used to reduce speckle in ultrasound images and to improve the SNR [12], [47]. Because the statistical nature of the backscattered echo signal arises from the relative locations of the scatterers with respect to the transducer that contribute to the echo signal, compounding can also be used to improve the statistical properties of QUS parameter estimates [48]. To obtain a reduction in estimate variation, a sample can be insonfied from different angles, yielding partially decorrelated realizations of echo signals. QUS estimates derived from different angles of view can then be averaged together to reduce estimate variation.

4.4.2.2 Simulations

Simulations were performed to examine the effects of angular compounding on estimate bias and variation. A cylindrical phantom with an average scatterer number

density of five scatterers per resolution cell was constructed and scanned from 128 different angles. Parameters using the envelope statistics model were estimated using small overlapping ROIs in each image. The estimates from each image were first spatially compounded based on the ROI overlap. Then, estimates from ROIs corresponding to the same location in each phantom were averaged together to produce fully compounded images. Subsets of the 128 images were used to study the effects of increasing the number of compounded images. The log compressed scatterer number density estimates are shown in Figure 4.15; the estimated model parameters are listed in Table 4.1.

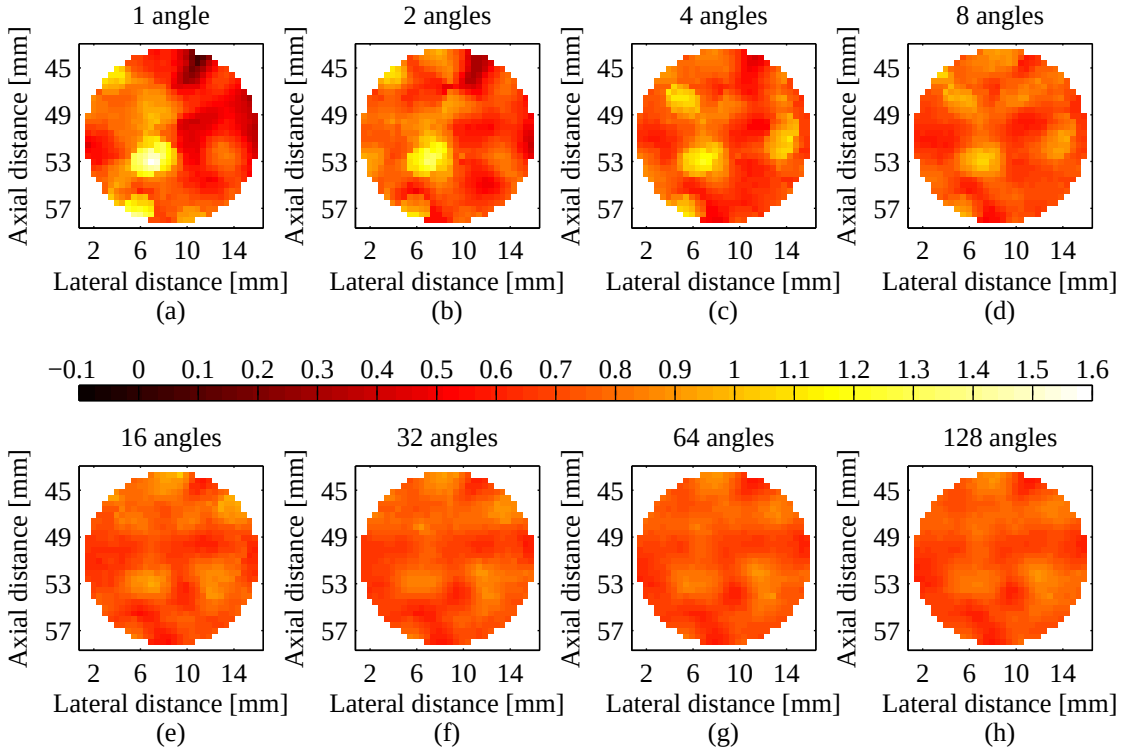

Figure 4.15. QUS images of the base 10 logarithm of the estimated scatterer number density for simulated phantom scans. All subplots share the same color scale shown in the middle of the figure. The base 10 logarithm of the actual scatterer number density is approximately 0.70.

The bias and SD of the μ parameter generally decrease as the number of compounded images increases. Note, however, that this effect becomes smaller as the

number of compounded images becomes large because the echo signals become increasingly correlated with each other due to the angular separation becoming smaller. The performance of the *k* parameter estimates is similar, i.e., the SD decreases monotonically as the number of compounded images increases.

Table 4.1. Model parameter estimates (mean±SD) using angular compounding for simulated phantom.

Number of compounded images	*k*	μ
1	0.537±0.17	6.17±4.4
2	0.589±0.14	5.93±2.6
4	0.568±0.098	5.94±2.1
8	0.553±0.076	5.73±1.4
16	0.560±0.061	5.57±1.1
32	0.560±0.052	5.50±0.88
64	0.561±0.048	5.43±0.79
128	0.562±0.048	5.47±0.78

For comparison, the scatterer number density was also exactly determined by directly counting the number of scatterers in each ROI in the phantom. Because the scatterers were randomly placed in the phantom with an average number density of five scatterers per resolution cell, some variability in the actual number of scatterers per resolution cell is expected. Using the number of scatterers in each ROI, the volume of the ROI, and the volume of the resolution cell, a theoretical scatterer number density was obtained for each ROI. To make the comparison valid, the ROIs used were the same as those used in the statistical analysis of the images. Furthermore, spatial compounding was performed in the same way as in the analysis of the QUS images obtained from the simulations. Using this analysis, a theoretical scatterer number density of 5.03±0.30 was deduced. For the case when 128 measurements were compounded, the correlation coefficient between the actual scatterer number density and the estimated scatterer number density in each ROI was found to be 0.465. This indicates that much of the

variation in the estimated scatterer number density can be explained by actual variation in the number of scatterers per resolution cell corresponding to each ROI from the phantom. Figure 4.16 shows QUS images for both the counted and estimated scatterer number densities as well as a scatter plot that compares the two measures on an ROI-by-ROI basis.

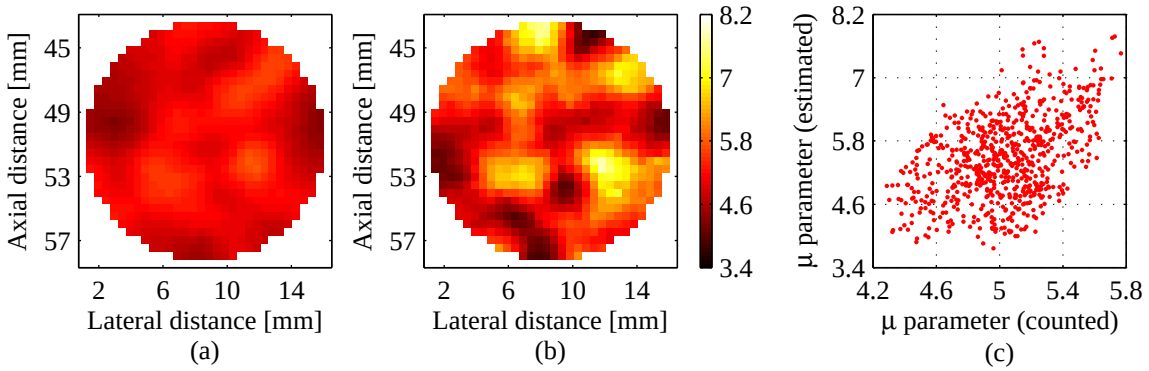

Figure 4.16. Comparison of deduced scatterer number density estimates: (a) QUS image of counted scatterer number density, (b) QUS image of estimated scatterer number density determined by averaging together estimates from 128 images, and (c) scatter plot of estimates from corresponding ROIs in (a) and (b). Subplots (a) and (b) share the same color scale.

4.4.2.3 Experimental phantom measurements

A physical phantom containing glass bead scatterers of mean radius 90 μm was constructed to experimentally verify the results of the simulations. The phantom was constructed with a 15% (by mass) concentration of gelatin in water. The scatterer concentration was 8.92 beads per cubic millimeter. The glass beads were assumed to be uniformly distributed throughout the phantom with random spatial locations.

The phantom was scanned with a focused (f/3) transducer with a center frequency of 5 MHz. The same transducer had been used to collect the data in Section 3.3.1. Referring to Table 3.1, the resolution cell volume was estimated to be 0.505 mm^3. Based on the resolution cell volume and the scatterer concentration, a scatterer number density of 4.50 scatterers per resolution cell was predicted. Data was acquired from 120 angles

uniformly distributed around the phantom. Because the axis of rotation of the phantom was not perfectly concentric with the center of the phantom, the images obtained from different angles of view were not registered. The equation of a circle describing the relative position of the center of the phantom as a function of the angle of rotation was derived. The images were registered by translating the images by the opposite of the amount of translation predicted by the equation for the circle.

Parameter estimation and spatial and angular compounding were performed in the same way as was used in the processing of the simulated data in the previous section. QUS images obtained by compounding subsets of the data are shown in Figure 4.17; the corresponding mean and SD of the envelope statistics model parameters are listed in Table 4.2.

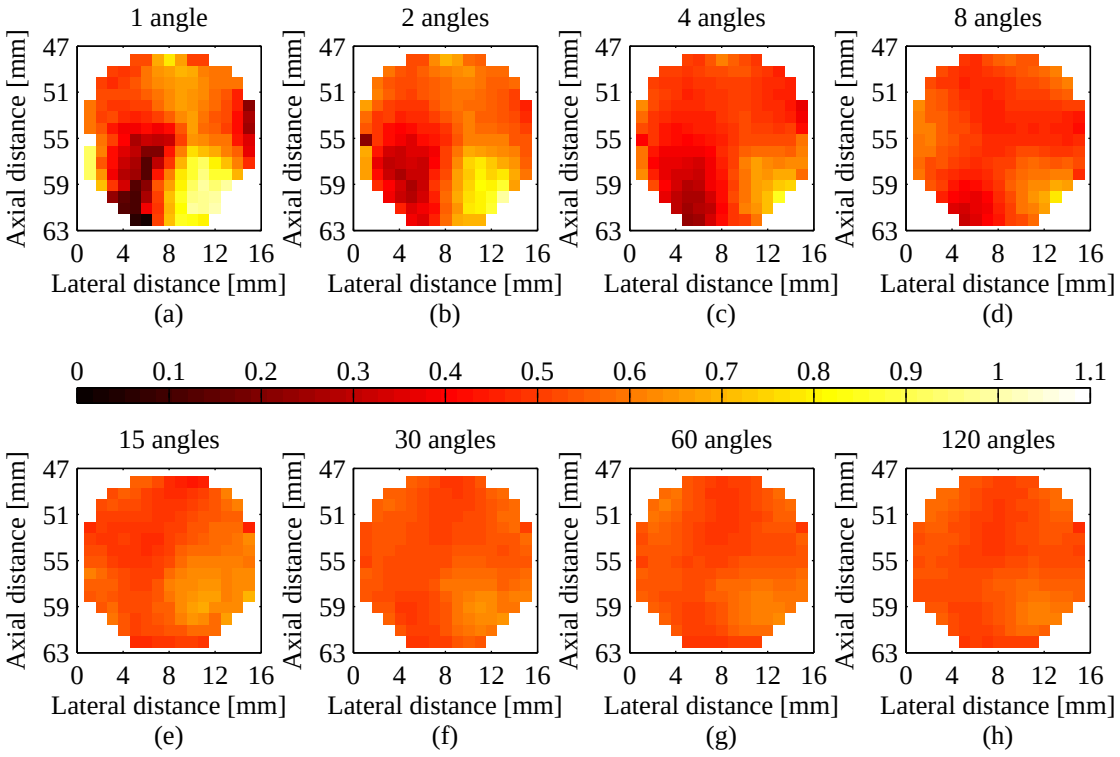

Figure 4.17. QUS images of the base 10 logarithm of the estimated scatterer number density for experimental phantom scans. All subplots share the same color scale shown in the middle of the figure.

Table 4.2. Model parameter estimates (mean±SD) using angular compounding for physical phantom.

Number of compounded images	k	μ
1	0.518±0.18	4.08±2.1
2	0.413±0.12	3.68±1.2
4	0.395±0.081	3.15±0.77
8	0.409±0.045	3.27±0.53
15	0.416±0.040	3.56±0.46
30	0.423±0.031	3.50±0.28
60	0.415±0.023	3.47±0.26
120	0.415±0.019	3.43±0.22

The results of the experiment and simulation are in excellent agreement. In both cases, the SD of the estimated model parameters decreases substantially as the number of angles of view increases. Based on the results of a previous study [48] that found an improvement in the SNR of QUS estimates that was proportional to the square root of the number of statistically independent images averaged together, it is reasonable to predict that the SD of the envelope statistics parameter estimates would also decrease accordingly. Figure 4.18 shows the SD of the two model parameter estimates versus the number of compounded images for both the simulated and experimental data. On a log-log plot, exponential functions appear as lines; therefore, for comparison, triangles are also plotted in Figure 4.18 with slope as predicted by the reciprocal of the square root of the number of compounded images.

The SD curves in Figure 4.18 do not follow the predicted slope exactly. When a small number (i.e., less than about 20) of images are compounded, the angular separation of the images is large enough that the QUS parameter estimates from each angle of view are statistically independent. As more angles of view are considered, the angular separation decreases. Once the point is reached where images are no longer statistically

independent, little improvement in estimate SD is expected. This effect was further quantified by calculating correlation coefficients of the QUS parameter estimates versus the angular separation of the images. To reduce the effects of noise, correlation coefficients were calculated for all pairs of images with a given angular separation and averaged together to produce an average correlation coefficient for that angular separation. These results are plotted in Figure 4.19 for both the simulated and experimental data. For both model parameters from the simulated data and for the μ parameter from the experimental data, the correlation coefficient increased dramatically for an angular separation of less than about 9º.

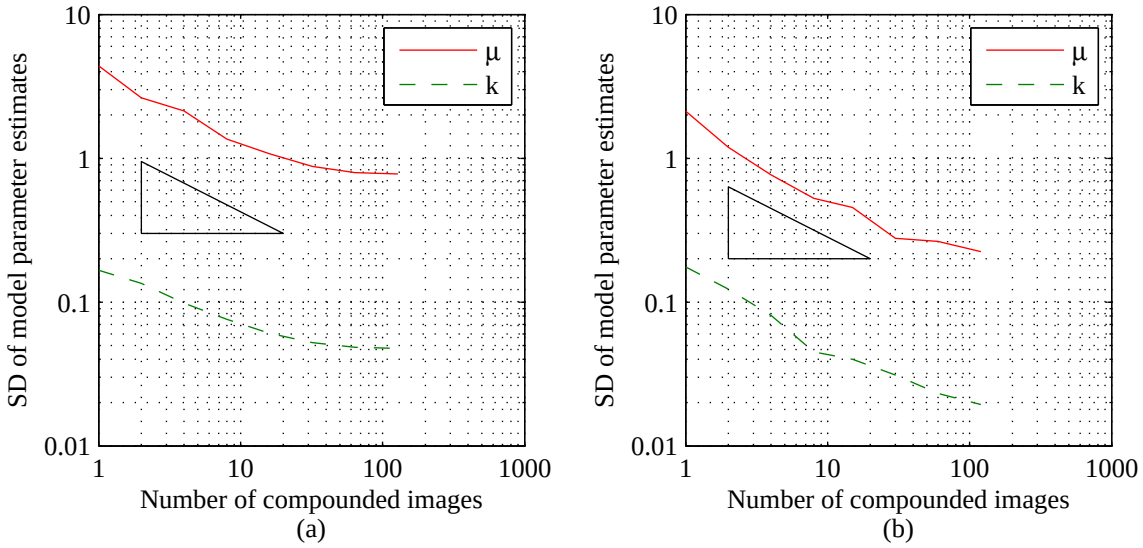

Figure 4.18. SD of envelope statistics parameter estimates versus the number of compounded images for (a) simulated data and (b) experimental data. Ideally, the SD of the estimates would lie on lines with the same slope as the hypotenuse of the triangle shown in each plot.

The substantial reduction in the SD of the parameter estimates suggests that angular compounding may be a powerful tool for tissue characterization and detection of disease. However, in practice, full 360º angular compounding is not possible for most of the human body. Nonetheless, partial compounding could be used almost anywhere to obtain some reduction in the SD of parameter estimates.

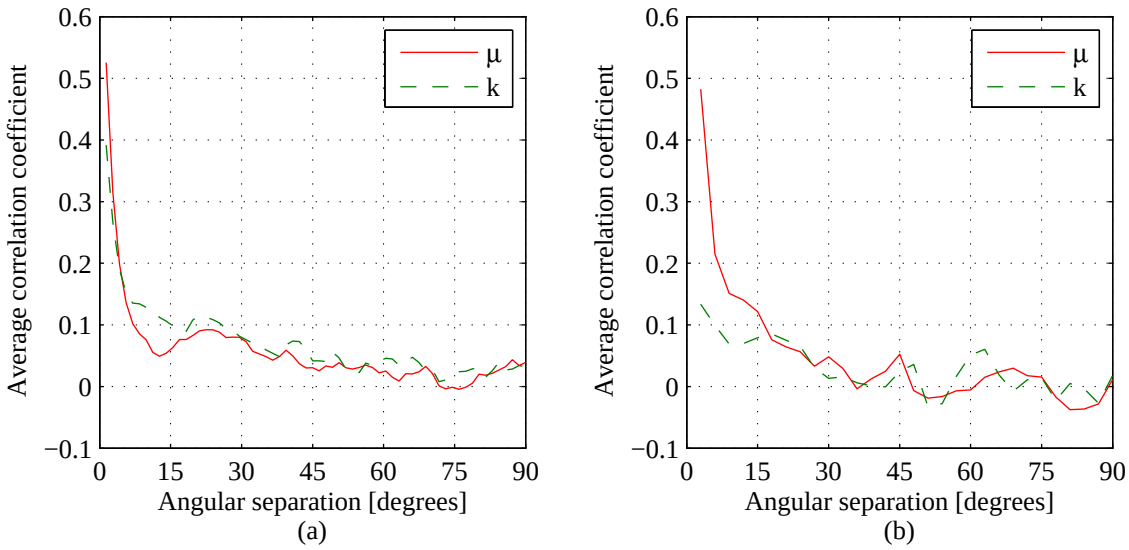

Figure 4.19. Average correlation coefficients of estimated model parameters versus the amount of angular separation between the images for (a) simulated data and (b) experimental data.

CHAPTER 5
CONCLUSIONS

While this is not the first work to address the subject of statistical models of backscattered ultrasound signals, it is hoped that the improved estimation methods will be useful for fast and accurate processing of backscattered ultrasound signals. The results of Chapter 4 should provide guidelines for the application and interpretation of statistical analyses. The benefits of the improved estimation algorithm come at the cost of using extra storage space for the data used in the estimation process. However, the space requirements are very modest, making this a worthwhile tradeoff.

The primary goal of this study was to assess the diagnostic potential of envelope-based statistics. The results of the study confirm that the statistical modeling of the envelope of backscattered ultrasound may be useful for the detection of disease. While statistically significant differences were observed between different kinds of tissue, further study is needed to better describe the correlation between tissue microstructure associated with disease and parameters derived from the envelope statistics model.

A new estimation algorithm has been developed to rapidly and accurately estimate parameters from the envelope statistics model. The algorithm has been tested using simulated and experimental data, and the bias and variance of the estimates versus region of interest size, spatial compounding, and angular compounding have been established.

5.1 Future Work

The estimation algorithm presented in Section 2.2 could be further modified and improved by choosing different classifier functions (Equation (2.20)) other than SNR, skewness, and kurtosis and by choosing different moment orders. The algorithm could be improved generically for a wide range of parameter values. Alternatively, following the observation in Section 2.3 that the present estimator is a general purpose estimator designed to work relatively well for a large range of parameter values, the estimator could be fine-tuned to work better for more specific ranges of parameter values. A multi-stage parameter estimator could be developed: preliminary parameter estimates could first be obtained using a general purpose estimator and then refined using a specific, fine-tuned estimator selected according to the preliminary parameter estimates.

As stated in Section 2.2.6.3, parameter estimates are selected using a grid search algorithm. To speed convergence and to provide further robustness against convergence to local minima, alternative optimization algorithms could be used. The basic procedure for determining level curves presented in Section 2.2.6.2 could be improved, i.e., better approximations of level curves could be found by interpolation.

APPENDIX A
SOLUTION TO SYSTEM OF EVEN MOMENT EQUATIONS

Although it is nonlinear, the system of even moment equations, Equations (2.1)-(2.3), does indeed have closed form solutions; however, they are very complicated. For simplicity, the system is solved in terms of the variables μ, s^2, and σ^2. Furthermore, the model parameters and solutions are allowed, in general, to be complex. For brevity, define

$$a = E\left[A^2\right] \tag{A.1}$$

$$b = E\left[A^4\right] \tag{A.2}$$

$$c = E\left[A^6\right] \tag{A.3}$$

Furthermore, to express the solutions in a simpler fashion, define several intermediate variables,

$$d = \left(80a^6 - 216a^4b + 201a^2b^2 - 64b^3 - 8a^3c + 6abc + c^2\right)^{1/3} \tag{A.4}$$

$$e = -4a^2 + 4b + d \tag{A.5}$$

$$f = \frac{4a^3 - 3ab - c}{2\sqrt{e}} \tag{A.6}$$

$$g = -\frac{3}{2}\left(a^2 - b\right) + \frac{1}{2}\left(-a^2 + b\right) - \frac{d}{4} \tag{A.7}$$

$$h = 16a^6 - 24a^4b - 15a^2b^2 + 16b^3 + 24a^3c - 18abc + c^2 \tag{A.8}$$

$$m = 8\left(4a^3 - 3ab - c\right)\left(\left(a^2 - 2b\right)b + ac\right) \tag{A.9}$$

$$p = 6\left(4a^3 - 5ab + c\right)^2\sqrt{e} \tag{A.10}$$

$$q = e\left(16a^5 + 20a^2c + ab\left(-12b + 15d - 5e\right) + 4a^3\left(-5b - 3d + e\right) + c\left(-4b - 3d + e\right)\right) \quad \text{(A.11)}$$

$$r = 16\left(4a^5 + 2a^2c - bc\right) \quad \text{(A.12)}$$

$$t = \sqrt{f + g} \quad \text{(A.13)}$$

$$v = \sqrt{-f + g} \quad \text{(A.14)}$$

$$x = -3cd + 4a^3\left(32b - 3d - 4g\right) - 4cg + ab\left(-48b + 15d + 20g\right) - r \quad \text{(A.15)}$$

$$y = -8\left(\left(a^2 - 2b\right)b + ac\right)\sqrt{e} - 4\left(4a^3 - 5ab + c\right) f \quad \text{(A.16)}$$

There are a total of four unique solutions. In terms of the intermediate variables, the first two solutions are given by

$$\mu = \frac{m + p + q}{4h\sqrt{e}} \pm \frac{v\left(x - y\right)}{2h} \quad \text{(A.17)}$$

$$s^2 = a + \frac{\sqrt{e}}{2} \mp v \quad \text{(A.18)}$$

$$\sigma^2 = \frac{1}{4}\left(-\sqrt{e} \pm 2v\right) \quad \text{(A.19)}$$

and the other two solutions are

$$\mu = -\frac{m - p + q}{4h\sqrt{e}} \pm \frac{t\left(x + y\right)}{2h} \quad \text{(A.20)}$$

$$s^2 = a - \frac{\sqrt{e}}{2} \mp t \quad \text{(A.21)}$$

$$\sigma^2 = \frac{1}{4}\left(\sqrt{e} \pm 2t\right) \quad \text{(A.22)}$$

It is straightforward, albeit tedious, to verify that these solutions are correct by substituting them back into Equations (2.1)-(2.3) and also substituting for the intermediate variables given by Equations (A.4)-(A.16).

REFERENCES

[1] J. M. Mamou, "Ultrasonic characterization of three animal mammary tumors from three-dimensional acoustic tissue models," Ph.D. dissertation, University of Illinois at Urbana-Champaign, Urbana, IL, 2005.

[2] W. N. McDicken, *Diagnostic Ultrasonics: Principles and Use of Instruments*. New York, NY: John Wiley & Sons, Inc., 1976.

[3] J. J. Wild and J. M. Reid, "Application of echo-ranging techniques to the determination of structure of biological tissues," *Science*, vol. 115, pp. 226-230, 1952.

[4] W. Huang, "Enhanced image quality reconstruction in medical ultrasound imaging," Ph.D. dissertation, University of Virginia, Charlottesville, VA, 2008.

[5] A. S. Tunis, "Monitoring structural changes in cells and tissues with high frequency ultrasound signal statistics," M.S. thesis, University of Toronto, Toronto, ON, Canada, 2005.

[6] M. F. Insana, "Ultrasonic imaging," in *Wiley Encyclopedia of Biomedical Engineering*, M. Akay, Ed. Hoboken, NJ: John Wiley & Sons, 2006, pp. 3640-3648.

[7] E. Jakeman and P. N. Pusey, "A model for non-Rayleigh sea echo," *IEEE Transactions on Antennas and Propagation*, vol. 24, pp. 806-814, 1976.

[8] R. F. Wagner, S. W. Smith, J. M. Sandrik, and H. Lopez, "Statistics of speckle in ultrasound B-scans," *IEEE Transactions on Sonics and Ultrasonics*, vol. 30, pp. 156-163, 1983.

[9] R. Barakat, "First-order statistics of combined random sinusoidal waves with applications to laser speckle patterns," *Optica Acta*, vol. 21, pp. 903-921, 1974.

[10] V. Dutt, "Statistical analysis of ultrasound echo envelope," Ph.D. dissertation, Mayo Graduate School, Rochester, MN, 1995.

[11] R. Smolíková, "Neural and statistical modeling of ultrasound backscatter," Ph.D. dissertation, University of Louisville, Louisville, KY, 2002.

[12] R. S. C. Cobbold, *Foundations of Biomedical Ultrasound*. New York, NY: Oxford University Press, 2007.

[13] T. Eltoft, "Modeling the amplitude statistics of ultrasonic images," *IEEE Transactions on Medical Imaging*, vol. 25, pp. 229-240, 2006.

[14] V. Dutt and J. F. Greenleaf, "Ultrasound echo envelope analysis using a homodyned K distribution signal model," *Ultrasonic Imaging*, vol. 16, pp. 265-287, 1994.

[15] G. E. Sleefe and P. P. Lele, "Tissue characterization based on scatterer number density estimation," *IEEE Transactions on Ultrasonics, Ferroelectrics, and Frequency Control*, vol. 35, pp. 749-757, 1988.

[16] E. Jakeman, "On the statistics of K-distributed noise," *Journal of Physics A: Mathematical and General*, vol. 13, pp. 31-48, 1980.

[17] D. M. Drumheller and H. Lew, "Homodyned-K fluctuation model," *IEEE Transactions on Aerospace and Electronic Systems*, vol. 38, pp. 527-542, 2002.

[18] P. M. Shankar, "A general statistical model for ultrasonic backscattering from tissues," *IEEE Transactions on Ultrasonics, Ferroelectrics, and Frequency Control*, vol. 47, pp. 727-736, 2000.

[19] P. H. Tsui and C. C. Chang, "Imaging local scatterer concentrations by the Nakagami statistical model," *Ultrasound in Medicine & Biology*, vol. 33, pp. 608-619, 2007.

[20] T. Eltoft, "The Rician inverse Gaussian distribution: A new model for non-Rayleigh signal amplitude statistics," *IEEE Transactions on Image Processing*, vol. 14, pp. 1722-1735, 2005.

[21] B. I. Raju and M. A. Srinivasan, "Statistics of envelope of high-frequency ultrasonic backscatter from human skin in vivo," *IEEE Transactions on Ultrasonics, Ferroelectrics and Frequency Control*, vol. 49, pp. 871-882, 2002.

[22] T. Eltoft, "A new approach to modeling signal amplitude statistics by the K distributions," in *Proceedings of the 7th Nordic Signal Processing Symposium*, 2006, pp. 62-65.

[23] M. P. Wachowiak, R. Smolíková, J. M. Zurada, and A. S. Elmaghraby, "Estimation of K distribution parameters using neural networks," *IEEE Transactions on Biomedical Engineering*, vol. 49, pp. 617-620, 2002.

[24] A. Mezache and F. Soltani, "A new approach for estimating the parameters of the K-distribution using fuzzy-neural networks," *IEEE Transactions on Signal Processing*, vol. 56, pp. 5724-5728, 2008.

[25] V. Dutt and J. F. Greenleaf, "Speckle analysis using signal to noise ratios based on fractional order moments," *Ultrasonic Imaging*, vol. 17, pp. 251-268, 1995.

[26] F. Ossant, F. Patat, M. Lebertre, M.-L. Teriierooiterai, and L. Pourcelot, "Effective density estimators based on the K distribution: Interest of low and fractional order moments," *Ultrasonic Imaging*, vol. 20, pp. 243-259, 1998.

[27] R. W. Prager, A. H. Gee, G. M. Treece, and L. H. Berman, "Analysis of speckle in ultrasound images using fractional order statistics and the homodyned k-distribution," *Ultrasonics*, vol. 40, pp. 133-137, 2002.

[28] M. Martin-Fernandez and C. Alberola-Lopez, "On low order moments of the homodyned-k distribution," *Ultrasonics*, vol. 43, pp. 283-290, 2005.

[29] K. A. Wear, R. F. Wagner, D. G. Brown, and M. F. Insana, "Statistical properties of estimates of signal-to-noise ratio and number of scatterers per resolution cell," *Journal of the Acoustical Society of America*, vol. 102, pp. 635-641, 1997.

[30] K. A. Wear and R. L. Popp, "Methods for estimation of statistical properties of envelopes of ultrasonic echoes from myocardium," *IEEE Transactions on Medical Imaging*, vol. MI-6, pp. 281-291, 1987.

[31] M. Martin-Fernandez, R. Cardenes, and C. Alberola-Lopez, "Parameter estimation of the homodyned K distribution based on signal to noise ratio," in *Proceedings of the IEEE Ultrasonics Symposium*, 2007, pp. 158-161.

[32] M. G. Bulmer, *Principles of Statistics*. Cambridge, MA: The M.I.T. Press, 1965.

[33] L. J. Slater, *Confluent Hypergeometric Functions*. Cambridge, UK: Cambridge University Press, 1960.

[34] M. T. Heath, *Scientific Computing: An Introductory Survey*, 2nd ed. New York, NY: McGraw-Hill, 2002.

[35] N. Rao, S. Mehra, and H. Zhu, "Ultrasound speckle statistics variations with imaging systems impulse response," in *Proceedings of the IEEE Ultrasonics Symposium*, 1990, pp. 1435-1440.

[36] V. Dutt and J. F. Greenleaf, "Adaptive speckle reduction filter for log-compressed B-scan images," *IEEE Transactions on Medical Imaging*, vol. 15, pp. 802-813, 1996.

[37] L. Weng, J. M. Reid, P. M. Shankar, and K. Soetanto, "Ultrasound speckle analysis based on the K distribution," *Journal of the Acoustical Society of America*, vol. 89, pp. 2992-2995, 1991.

[38] M. L. Oelze and W. D. O'Brien, Jr., "Defining optimal axial and lateral resolution for estimating scatterer properties from volumes using ultrasound backscatter," *Journal of the Acoustical Society of America*, vol. 115, pp. 3226-3234, 2004.

[39] R. F. Wagner, M. F. Insana, and S. W. Smith, "Fundamental correlation lengths of coherent speckle in medical ultrasonic images," *IEEE Transactions on Ultrasonics, Ferroelectrics and Frequency Control*, vol. 35, pp. 34-44, 1988.

[40] A. Abdi and M. Kaveh, "Performance comparison of three different estimators for the Nakagami m parameter using Monte Carlo simulation," *IEEE Communications Letters*, vol. 4, pp. 119-121, 2000.

[41] J. G. Proakis, *Digital Communications*. New York, NY: McGraw-Hill, 1983.

[42] J. A. Jensen, "Field: A program for simulating ultrasound systems," *Medical & Biological Engineering & Computing*, vol. 34, supplement 1, part 1, pp. 351-353, 1996.

[43] J. A. Jensen and N. B. Svendsen, "Calculation of pressure fields from arbitrarily shaped, apodized, and excited ultrasound transducers," *IEEE Transactions on Ultrasonics, Ferroelectrics, and Frequency Control*, vol. 39, pp. 262-267, 1992.

[44] X. Hao, C. J. Bruce, C. Pislaru, and J. F. Greenleaf, "Characterization of reperfused infarcted myocardium from high-frequency intracardiac ultrasound imaging using homodyned K distribution," *IEEE Transactions on Ultrasonics, Ferroelectrics, and Frequency Control*, vol. 49, pp. 1530-1542, 2002.

[45] K. Raum and W. D. O'Brien, Jr., "Pulse-echo field distribution measurement technique for high-frequency ultrasound sources," *IEEE Transactions on Ultrasonics, Ferroelectrics, and Frequency Control*, vol. 44, pp. 810-815, 1997.

[46] J. A. Zagzebski, J.-F. Chen, F. Doug, and T. Wilson, "Intervening attenuation affects first-order statistical properties of ultrasound echo signals," *IEEE Transactions on Ultrasonics, Ferroelectrics, and Frequency Control*, vol. 46, pp. 35-40, 1999.

[47] C. B. Burckhardt, "Speckle in ultrasound B-mode scans," *IEEE Transactions on Sonics and Ultrasonics*, vol. 25, pp. 1-6, 1978.

[48] A. L. Gerig, T. Varghese, and J. A. Zagzebski, "Improved parametric imaging of scatterer size estimates using angular compounding," *IEEE Transactions on Ultrasonics, Ferroelectrics, and Frequency Control*, vol. 51, pp. 708-715, 2004.